

Unraveling information about supranuclear-dense matter from the complete binary neutron star coalescence process using future gravitational-wave detector networks

Anna Puecher^{1,2}, Tim Dietrich^{3,4}, Ka Wa Tsang^{1,2,5}, Chinmay Kalaghatgi^{1,2,6}, Soumen Roy^{1,2},
Yoshinta Setyawati^{1,2}, and Chris Van Den Broeck^{1,2}

¹*Nikhef—National Institute for Subatomic Physics, Science Park 105,
1098 XG Amsterdam, The Netherlands*

²*Institute for Gravitational and Subatomic Physics (GRASP), Utrecht University,
Princetonplein 1, 3584 CC Utrecht, The Netherlands*

³*Institut für Physik und Astronomie, Universität Potsdam, Haus 28, Karl-Liebknecht-Straße 24/25,
14476 Potsdam, Germany*

⁴*Max Planck Institute for Gravitational Physics (Albert Einstein Institute),
Am Mühlenberg 1, 14476 Potsdam, Germany*

⁵*Van Swinderen Institute for Particle Physics and Gravity, University of Groningen,
Nijenborgh 4, 9747 AG Groningen, The Netherlands*

⁶*Institute for High-Energy Physics, University of Amsterdam, Science Park 904,
1098 XH Amsterdam, The Netherlands*

 (Received 18 October 2022; accepted 10 May 2023; published 7 June 2023)

Gravitational waves provide us with an extraordinary tool to study the matter inside neutron stars. In particular, the postmerger signal probes an extreme temperature and density regime and will help reveal information about the equation of state of supranuclear-dense matter. Although current detectors are most sensitive to the signal emitted by binary neutron stars before the merger, the upgrades of existing detectors and the construction of the next generation of detectors will make postmerger detections feasible. For this purpose, we present a new analytical, frequency-domain model for the inspiral-merger-postmerger signal emitted by binary neutron star systems. The inspiral and merger parts of the signals are modeled with `IMRPhenomD_NRTidalv2`, and we describe the main emission peak of the postmerger with a three-parameter Lorentzian, using two different approaches: one in which the Lorentzian parameters are kept free, and one in which we model them via quasiuniversal relations. We test the performance of our new complete waveform model in parameter estimation analyses, studying simulated signals obtained both from our developed model and by injecting numerical relativity waveforms. We investigate the performance of different detector networks to determine the improvement that future detectors will bring to our analysis. We consider Advanced LIGO+ and Advanced Virgo+, KAGRA, and LIGO-India. We also study the possible impact of a detector with high sensitivity in the kilohertz band like NEMO, and finally we compare these results to the ones we obtain with third-generation detectors, the Einstein Telescope and the Cosmic Explorer.

DOI: [10.1103/PhysRevD.107.124009](https://doi.org/10.1103/PhysRevD.107.124009)

I. INTRODUCTION

Neutron stars (NSs) can reach extremely high densities, creating conditions that cannot be reproduced by laboratory experiments. Hence, they provide a perfect environment to study supranuclear-dense matter and its equation of state (EOS). Until a few years ago, the study of NSs was limited to electromagnetic (EM) observations, but since the first detection of a gravitational-wave (GW) signal from a binary neutron star (BNS), GW170817 [1], GWs provide new ways to study NSs and their mergers. Since the EOS determines the NS's macroscopic properties, such as its mass, radius, and tidal deformability, it can be constrained by measuring the imprint it leaves in the GW signal emitted during the coalescence [2,3].

Up to now, Advanced LIGO [4] and Advanced Virgo [5] detected two BNS systems, GW170817 [1,6] and GW190425 [7]. These detections already allowed us to put constraints on the supranuclear-dense matter EOS, which was possible, since the GW signal emitted during the inspiral phase provides information about the EOS through tidal deformability measurements [2,8–16]. While the uncertainty on current measurements is still large, the higher sensitivities of future-generation detectors such as the Einstein Telescope (ET) [17–23] or the Cosmic Explorer (CE) [24,25] will significantly improve them.

In addition to a more detailed analysis of the inspiral phase, third-generation (3G) GW detectors such as ET and CE are also expected to detect GWs from the postmerger

phase of the BNS coalescence [26–30]. This is of special interest, since the postmerger phase probes an even higher different density and temperature regime than the inspiral phase. During the inspiral phase, only densities up to the central density of the individual stars are probed, which corresponds to about 3 to 4 times the nuclear saturation density, while the postmerger phase probes densities even beyond 5 times the nuclear saturation density; cf. Fig. 1 of Ref. [31]. In addition, temperatures of about 50 MeV are reached during the postmerger phase, which is large enough that the effects of different transport coefficients will start to impact the data [32–34].

Unfortunately, postmerger studies pose numerous challenges. First, the amplitude of the GW strain of the postmerger part of the observed GW signal is expected to be weaker than that of the inspiral one [35–39]. Second, at higher frequencies, the detectors’ sensitivity drops due to quantum shot noise. For these reasons, it is not surprising that the dedicated searches for GWs emitted by a possible remnant of GW170817 [40,41] found no evidence of such a signal and showed that with the sensitivity of Advanced LIGO and Advanced Virgo, the source distance should have been at least 1 order of magnitude less for the postmerger signal to be detectable. Finally, postmerger physics includes thermal effects, magnetohydrodynamical instabilities, neutrino emission, dissipative processes, and possible phase transitions [42–48], which make the postmerger particularly difficult to model, but on the other hand allow us to investigate a variety of interesting physical processes. Because of the complexity of the evolution, the study of the postmerger relies heavily on numerical relativity (NR) simulations, which, however, are also limited due to their high computational cost and the fact that it is currently not possible to take into account all the physical processes that influence the postmerger.

Nonetheless, previous studies based on NR simulations showed some common key features of the postmerger GW spectrum, finding in some cases universal relations with the NS properties [36–39,49–57], and some efforts have also been made to construct full inspiral, merger, and postmerger models for BNS coalescences. Also, morphology-independent analyses of the postmerger GW signal have been proposed in Refs. [51,56,58], while in Ref. [59] a hierarchical model to generate postmerger spectra was developed. With a different approach, Refs. [60–62] construct analytical models for the postmerger signal, based on features found in NR simulated waveforms. Breschi *et al.* in Ref. [63] propose a frequency-domain model for the postmerger, built with a combination of complex Gaussian wavelets, and show in Ref. [64] how this model performs using a 3G detector network. Wijngaarden *et al.* [65] build a hybrid model, using analytical templates for the premerger phase and a morphology-independent analysis, based on sine-Gaussian wavelets, for the postmerger phase.

Following similar ideas, in this paper we construct a phenomenological frequency-domain model for the entire

BNS coalescence consisting of the inspiral, merger, and postmerger phases. Our final aim is to employ the developed model for parameter estimation analyses. To model the coalescence during the inspiral up to the merger, we rely on IMRPhenomD_NRTidalv2 [66]. The postmerger phase is modeled with a three-parameter Lorentzian describing the main emission peak of its spectrum, following Tsang *et al.* [67]. For the Lorentzian, we use two different approaches: in one case, we compute the parameters from quasiuniversal relations, describing them as a function of the BNS’s properties; in the other one, we treat them as free parameters. Both versions can be directly employed by existing parameter estimation pipelines; see, e.g., Refs. [68,69].

This paper is structured as follows: In Sec. II, we describe how our model is built, the methods used for parameter estimation, and the detectors we consider. Results are shown in Sec. III, and conclusions are presented in Sec. IV. Appendix A shows the results obtained specifically with our postmerger model with free Lorentzian parameters; in Appendix B we discuss general parameter estimation with future detectors; and in Appendix C we provide more details about the validity and settings of the methods employed for our study.

II. METHODS AND SETUP

We construct a frequency-domain waveform model to describe the full inspiral, merger, and postmerger phases of a BNS coalescence. In this section, we describe how we model the postmerger part of the signal, and how we connect it to the inspiral-merger model to obtain the full waveform. We then describe the framework used for data analysis, explaining how we speed up parameter estimation using relative binning, the analysis setup, the BNS sources that we study, and the employed detector networks to determine to what extent future detector networks will enable postmerger studies.

A. Inspiral-merger-postmerger model construction

Multiple studies have shown that the postmerger GW spectrum includes various strong peaks [36–39,49,52–55,70]. For simplicity, we limit ourselves to the main emission peak at a frequency f_2 , which corresponds to the dominant GW frequency; see, e.g., Ref. [49]. Following this approach, the postmerger signal can be described in the time domain by a simple damped sinusoidal waveform [67], whose Fourier transform is a Lorentzian. Therefore, in the frequency domain, we model the postmerger phase with a three-parameter Lorentzian,

$$h_{22}(f) = \frac{c_0 c_2}{\sqrt{(f - c_1)^2 + c_2^2}} e^{-i \arctan(\frac{f - c_1}{c_2})}, \quad (1)$$

where c_0 corresponds to the maximum value, c_1 to the dominant emission frequency f_2 , and c_2 to the inverse of the damping time, which sets the Lorentzian’s width.

We determine the coefficients c_i with two different approaches: (I) we treat them as free parameters and try to measure c_0 , c_1 , and c_2 together with the BNS's other properties; and (II) we compute the c_i coefficients from quasiuniversal relations that describe them as functions of the system's parameters. Depending on its properties and the EOS, a given BNS could undergo a prompt collapse to a black hole (BH), and hence be without a postmerger emission. In this scenario, while in case I we expect that the values recovered for the free parameters will reflect the absence of a postmerger signal, in case II the quasiuniversal relations employed might lead to a bias in the estimation of the binary's intrinsic parameters. For this reason, we ideally want to use the Lorentzian model with quasiuniversal relations only when we know that a postmerger emission is present. Since the threshold mass for a prompt collapse is EOS dependent and still unknown, following Ref. [60], we assume that a BNS system undergoes prompt collapse if the tidal polarizability parameter κ_2^T is lower than a threshold value $\kappa_{\text{thr}} = 40$. The quantity κ_2^T is defined as

$$\kappa_2^T = 3[\Lambda_2^A(X_A)^4 X_B + \Lambda_2^B(X_B)^4 X_A], \quad (2)$$

where $\Lambda_2^j = \frac{2}{3}k_2(R_j/M_j)^5$ with $j \in \{A, B\}$ are the dimensionless tidal deformabilities, and $X_j = M_j/M$. Here, k_2 is the dimensionless $\ell = 2$ Love number; R_j and M_j are the radius and gravitational mass of the individual stars, respectively; and $M = M_A + M_B$ is the BNS's total mass.¹

1. Quasiuniversal relations for the Lorentzian parameters

For the approach introduced as method II, we use quasiuniversal relations—i.e., phenomenological relations that are independent of the EOS—to constrain the coefficients c_i in Eq. (1). This provides a direct connection between the Lorentzian coefficients and the BNS's properties.

Since the postmerger Lorentzian model extends the waveform used for inspiral and merger beyond its merger frequency f_{merg} , a straightforward way to find the value of c_0 is by rescaling the amplitude of the `IMRPhenomD_NRTidalv2` waveform at merger $\mathcal{A}_{\text{NRTidalv2}}(f_{\text{merg}})$. Specifically, we use

$$c_0 = \sigma \times \mathcal{A}_0 \times \mathcal{A}_{\text{NRTidalv2}}(f_{\text{merg}}), \quad (3)$$

where \mathcal{A}_0 is the mass and distance scaling factor employed in `IMRPhenomD` [72]. The prefactor σ is added to obtain a better calibration to the NR waveforms, and we set $\sigma = 10.0$, which gives the lowest mismatch values (the definition of mismatch and details about its computation are provided in Sec. II B).

¹See also Ref. [71] for more updated relations which were not yet available when we started our work.

Since c_1 represents the dominant postmerger oscillation frequency f_2 , we resort to the fit in Eq. (8) of Ref. [67]:

$$Mc_1(\zeta) = \beta \frac{1 + A\zeta}{1 + B\zeta}, \quad (4)$$

with $\beta = 3.4285 \times 10^{-2}$, $A = 2.0796 \times 10^{-3}$, and $B = 3.9588 \times 10^{-3}$. The parameter ζ is

$$\zeta = \kappa_{\text{eff}}^T - 131.7010 \frac{M}{M_{\text{TOV}}}. \quad (5)$$

In the last equation, $\kappa_{\text{eff}}^T = 3/18\tilde{\Lambda}$, with $\tilde{\Lambda}$ being the binary's mass-weighted tidal deformability

$$\tilde{\Lambda} = \frac{16(M_A + 12M_B)M_A^4\Lambda_A + (M_B + 12M_A)M_B^4\Lambda_B}{3(M_A + M_B)^5}. \quad (6)$$

Although ζ , and therefore c_1 , in Eq. (5) is a function of the maximum mass allowed for a nonrotating stable NS M_{TOV} , which depends on the specific EOS, we fix $M_{\text{TOV}} = 2M_{\odot}$ for the model version with quasiuniversal relations in this work.² The median relative error introduced on ζ by this approximation is 0.31, for the hybrid waveforms in the SACRA and CoRe database. This error propagates to the c_1 parameter, causing a median relative error of approximately 5%.

With this choice for c_0 and c_1 , a model for c_2 is built from a set of 48 nonspinning NR waveforms from the CoRe database [77,78]. For this, we first find the values of c_2 that minimize the mismatch of the Lorentzian waveform and the NR waveform between 0.75 c_1 and 8192 Hz using a flat noise power spectral density (PSD); see Sec. II B for details. The flat PSD ensures that no high-frequency information is suppressed in the match computation. For each waveform, c_2 minimization is performed using the “L-BFGS-B,” “SLSQP,” “TNC,” and “Powell” methods available in SciPy [79], and the value of c_2 with the smallest mismatch value is used. It can be seen that c_2 shows a similar trend against $\kappa_{\text{eff}}^T q^2$, with $q = M_A/M_B$ the mass ratio, as c_1 does against ζ . Hence, an analogous ansatz was used to perform a fit. However, using the parameters obtained from performing a simple curve fit showed unphysical amplitude behavior for a few of the NR waveforms. For further tuning, the mismatch was minimized for

²In principle, we could treat M_{TOV} as a free parameter, but this would impair the main benefit of this version of the model—namely, to avoid additional parameters to sample over. However, in the future, given the increasing number of multimessenger detections of binary neutron star mergers and the possibility to observe high-mass pulsars [73–76], one can expect to have a significantly smaller uncertainty in M_{TOV} than today. The value of the maximum supported mass estimated from this new information will then provide the fixed value of M_{TOV} to employ in our model.

all the NR waveforms by varying the fit parameters, and the parameters that gave the lowest mismatch were then recorded and added to the model. The functional form of c_2 and the values obtained for the fit parameters in this manner are

$$c_2 = 2 + \gamma \frac{1 + C\kappa_{\text{eff}}^T q^2}{1 + D\kappa_{\text{eff}}^T q^2}, \quad (7)$$

with $\gamma = 19.4579017$, $C = -9.63390738 \times 10^{-4}$, and $D = 6.45926154 \times 10^{-5}$. The median relative error for c_2 during minimization is 0.56.

2. The full waveform

To obtain a model describing the full coalescence, the previously derived postmerger model is connected to the waveform describing the inspiral and merger parts of the signal, for which we use the phenomenological waveform IMRPhenomD_NRTidalv2 [66].

Amplitude: To ensure a smooth transition³ between the two models, we apply a Planck-taper window α_{Pl} :

$$\alpha_{\text{Pl}} = \begin{cases} 0 & \text{for } f < f_{\text{tr}}, \\ \exp\left[\frac{f_{\text{end}} - f_{\text{tr}}}{f - f_{\text{tr}}} + \frac{f_{\text{end}} - f_{\text{tr}}}{f - f_{\text{end}}} + 1\right]^{-1} & \text{for } f_{\text{tr}} < f < f_{\text{end}}, \\ 1 & \text{for } f > f_{\text{end}}. \end{cases} \quad (8)$$

The window is applied just before the frequency of the main postmerger peak f_2 , which corresponds to our model's parameter c_1 . The value of the window's starting frequency f_{tr} is chosen to ensure a good match with NR waveforms. In particular, in Ref. [67], one of the time-domain features identified in the postmerger signal morphology is the *first postmerger minimum*, which corresponds to a clear amplitude minimum present shortly after the merger, before the amplitude starts increasing again. By comparison with NR waveforms in the CoRe database [77,78], we find that this feature is best reproduced by our model when the Planck

window is applied between $f_{\text{tr}} = 0.75c_1$ and $f_{\text{end}} = 0.9c_1$. Following Ref. [72], we add an exponential correction factor, $\exp[-\frac{p(f-c_1)}{c_2}]$, to the Lorentzian amplitude, in order to smoothen possible kinks arising when going to the time domain. We set $p = 0.01$, which is enough to reduce the kink, but not so large that it significantly influences the merger amplitude.

Phase: To ensure that the waveform phase is C^1 continuous, we introduce two coefficients a and b , writing the phase as

$$\phi_{\text{IM}}(f) = \phi_{\text{Lor}}(f) + a + bf, \quad (9)$$

with ϕ_{IM} being the phase of the IMRPhenomD_NRTidalv2 waveform and $\phi_{\text{Lor}} = \arg(h_{22}(f))$ that of the Lorentzian one.

The values of a and b are computed at the same transition frequency, $f_{\text{tr}} = 0.75c_1$, at which we start the Planck-taper window for the amplitude, such that

$$\left. \frac{d\phi_{\text{IM}}}{df} \right|_{f_{\text{tr}}} = \left. \frac{d\phi_{\text{Lor}}}{df} \right|_{f_{\text{tr}}} + b, \quad (10)$$

$$\phi_{\text{IM}}(f_{\text{tr}}) = \phi_{\text{Lor}}(f_{\text{tr}}) + bf_{\text{tr}} + a. \quad (11)$$

Finally, to reduce the Lorentzian contribution to the premerger and merger amplitude, we multiply the waveform by a factor $\exp[-i2\pi\Delta t f]$, which will induce a time shift of Δt in the time-domain waveform; Δt is computed as the time interval between the merger and the *first postmerger minimum* described by Eq. (2) in Ref. [67].

The frequency-domain gravitational waveform can be written as

$$\tilde{h}(f) = \mathcal{A}(f)e^{i\phi(f)}, \quad (12)$$

with $\mathcal{A}(f)$ being the amplitude and $\phi(f)$ the phase. Therefore, in our model, the full waveform is given by

$$\tilde{h}(f) = \begin{cases} \mathcal{A}_{\text{IM}}(f)e^{i\phi_{\text{IM}}} & \text{for } f < f_{\text{tr}}, \\ \left(\mathcal{A}_{\text{IM}}(f) + \alpha_{\text{Pl}}\mathcal{A}_{\text{Lor}}(f)e^{-\frac{p(f-c_1)}{c_2}}\right)e^{i(\phi_{\text{Lor}}+bf+a)-i2\pi\Delta t f} & \text{for } f > f_{\text{tr}}, \end{cases} \quad (13)$$

where $\mathcal{A}_{\text{IM}}(f)$ and $\phi_{\text{IM}}(f)$ are the amplitude and phase, respectively, of the IMRPhenomD_NRTidalv2 waveform, and $\mathcal{A}_{\text{Lor}} = |h_{22}(f)|$ is the amplitude of the Lorentzian one.

In the following, we refer to the IMRPhenomD_NRTidalv2_Lorentzian postmerger model with quasiuniversal relations as QU-PM, to the model with free

Lorentzian parameters as FREE-PM, and to the model without a postmerger phase, IMRPhenomD_NRTidalv2, as NO-PM.

B. Mismatch

The mismatch between two waveforms h_1 and h_2 is defined as

$$MM = 1 - \max_{\phi_c, t_c} \frac{\langle h_1(\phi_c, t_c) | h_2 \rangle}{\sqrt{\langle h_1 | h_1 \rangle \langle h_2 | h_2 \rangle}}, \quad (14)$$

³We note that the employed approach neglects any contribution of the postmerger signal toward frequencies below the merger frequency.

where t_c and ϕ_c are an arbitrary time and phase shift, and the noise-weighted inner product is defined as

$$\langle a|b \rangle \equiv 4\text{Re} \int_{f_{\text{low}}}^{f_{\text{high}}} \frac{\tilde{a}^*(f)\tilde{b}(f)}{S_n(f)} df, \quad (15)$$

where $S_n(f)$ is the noise spectral density, $\tilde{a}(f)$ is the Fourier transform of $a(t)$, and $*$ denotes the complex conjugate. To validate the IMRPhenomD_NRTidalv2_Lorentzian model, we compute mismatches with the hybrid waveforms in the CoRe [77,78] and SACRA [80] databases. The mismatch is computed with PyCBC [81] functions and zero noise—i.e., with a flat PSD. For the FREE-PM model, to get the Lorentzian parameters that better describe each hybrid's postmerger, we optimize the mismatch over c_1, c_2 ; we do not include the Lorentzian maximum value c_0 in the minimization, because, giving just an amplitude scaling factor, the mismatch is insensitive to it. The initial values for the optimization are found with a least-squares fit on the postmerger part of the hybrid waveform, for $f \geq 1.3f_{\text{merg}}$. Fixing c_1 and c_2 to the optimal values, we then compute the optimal value for c_0 with a least-square fit on the hybrid's postmerger signal. We use the optimal values for the c_i coefficients to generate the FREE-PM waveform, for which we compute the mismatch with the hybrid in different frequency ranges. For the QU-PM model, instead, the Lorentzian parameters are computed from the quasiuniversal relations described in Sec. II A 1, using the values of the hybrids' binary parameters. The top panel of Fig. 1 shows the mismatches in the frequency band $[1.1f_{\text{merg}}, 4096]$ Hz: despite our simple description of the postmerger, when using

the FREE-PM model for almost all hybrids, mismatches lie below 0.3. Mismatch values increase systematically by roughly a factor of 3 when computing them with respect to the QU-PM model, which is expected, since in this case the Lorentzian parameters are not optimized to the hybrid waveform. When considering the whole waveform, in the frequency range $[30, 4096]$ Hz, the mismatch is always below 0.005, as shown in the bottom panel of Fig. 1. Also in this case, for most hybrids, the FREE-PM model gives better matches compared to the QU-PM one. The fact that mismatches computed over the whole waveform do not follow the trend of the ones computed only in the high-frequency region is due to the fact that different values of the Lorentzian parameters translate also into different tapering and continuity conditions, influencing the late inspiral-merger phase too. For comparison, we show also the mismatches computed in the same frequency range with the NO-PM waveform. The plot does not highlight a systematic improvement in the mismatches when using one of the models; the difference between the mismatches obtained with the NO-PM and FREE-PM models varies from 0.0019 to 8×10^{-6} , with an average variation of 0.0005 . In some cases, the NO-PM model gives lower mismatches than one of the models with postmerger: this occurs because the NO-PM waveform includes no signal after the merger. Therefore, computing the mismatch for frequencies higher than the merger one, in a region where the waveform is zero, does not contribute to the overall mismatch; hence, the lack of the postmerger signal does not reduce the match computed up to the merger frequency. However, in more than 60% of cases, the mismatch is reduced when using the FREE-PM model, showing that our postmerger description with optimized parameters improves the signal characterization.

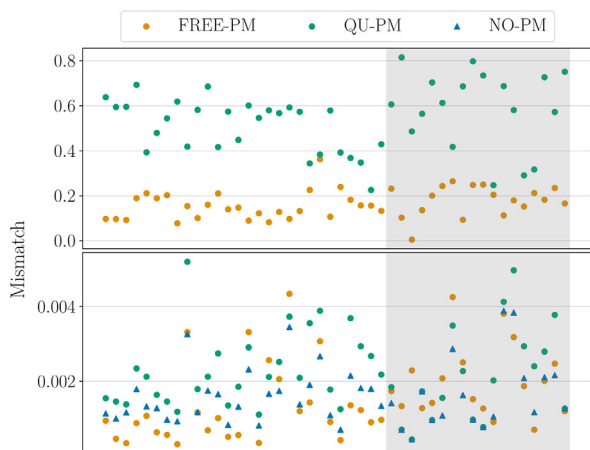


FIG. 1. Mismatches between hybrid waveforms from the CoRe (in the gray background band) and SACRA databases, and our postmerger model, for both the versions FREE-PM and QU-PM. The top panel shows mismatches in the postmerger frequency band (i.e., within $[1.1f_{\text{merg}}, 4096]$ Hz), while the bottom panel shows mismatches for the whole waveform (within $[30, 4096]$ Hz). In the latter case, for comparison we also show mismatches computed between the hybrids and the NO-PM model.

C. Parameter estimation

In the following, we focus on how to recover the source's parameters given the detector data d and under the hypothesis of a specific model \mathcal{H} used to describe the waveform. In a Bayesian framework, this corresponds to evaluating the posterior $p(\vec{\theta}|\mathcal{H}, d)$, which, according to Bayes' theorem, is

$$p(\vec{\theta}|\mathcal{H}, d) = \frac{p(d|\mathcal{H}, \vec{\theta})p(\vec{\theta}|\mathcal{H})}{p(d|\mathcal{H})}. \quad (16)$$

In Eq. (16), the prior probability density $p(\vec{\theta}|\mathcal{H})$ encodes our prior knowledge about the source or the model: the evidence $p(d|\mathcal{H})$ describes the probability of observing the data d given the model \mathcal{H} , independently of the specific choice of parameters $\vec{\theta}$; and the likelihood $p(d|\mathcal{H}, \vec{\theta})$ represents the probability of observing d with the specific set of parameters $\vec{\theta}$.

The priors chosen for this work are described later in this section, while the evidence $p(d|\mathcal{H})$ serves as the

normalization constant of the posterior distribution, and is given by

$$p(d|\mathcal{H}) = \int d\vec{\theta} p(d|\mathcal{H}, \vec{\theta}) p(\vec{\theta}|\mathcal{H}). \quad (17)$$

Assuming the data d consist of Gaussian noise and a GW signal $h(\vec{\theta})$, the likelihood can be expressed as [82]

$$p(d|\mathcal{H}, \vec{\theta}) \propto \exp \left[-\frac{1}{2} \langle d - h(\vec{\theta}) | d - h(\vec{\theta}) \rangle \right], \quad (18)$$

with the noise-weighted inner product defined as in Eq. (15).

To sample the likelihood function, we use the nested sampling [82,83] package DYNESTY [84,85], which is included in the `bilby` library [68,69], with 2048 live points.

1. Relative binning

The likelihood evaluations required at each sampling step are very expensive, since, in order to compute the inner product, we need to evaluate the waveform on a dense and uniform frequency grid. The size of the grid increases both with the duration of the signal and with the maximum frequency used in the analysis. In our case, we set $f_{\max} = 4096$ Hz, since the postmerger GW signal is expected to lie within the few-kilohertz regime. Moreover, we study BNS systems, whose low masses imply a long signal duration. Although we set the starting frequency to $f_{\text{low}} = 30$ Hz, the typical duration of the signal in band is still roughly 200 s. To overcome the issue of the computational cost of the analysis needed for this work, we employ the technique of relative binning [86,87], which reduces the number of waveform evaluations from all the points on the grid to a limited number of frequency bins.

The underlying assumption in relative binning is that the set of parameters yielding a non-negligible contribution to the posterior probability produce similar waveforms, such that their ratio varies smoothly in the frequency domain. In each frequency bin $b = [f_{\min}(b), f_{\max}(b)]$, if we choose a reference waveform $h_0(f)$ that describes sufficiently well the data, the ratio with the sampled waveforms can be approximated with a linear interpolation

$$\begin{aligned} r &= \frac{h(f)}{h_0(f)} \\ &= r_0(h, b) + r_1(h, b)(f - f_m(b)) \\ &\quad + \mathcal{O}[(f - f_m(b))^2], \end{aligned} \quad (19)$$

with $f_m(b)$ being the central frequency of the bin b .

This allows us to approximate the likelihood inner product as

$$\langle d(f) | h(f) \rangle \approx \sum_b (A_0(b) r_0^*(h, b) + A_1(b) r_1^*(h, b)), \quad (20)$$

where the summary data

$$A_0(b) = 4 \sum_{f \in b} \frac{d(f) h_0^*(f)}{S_n(f)/T}, \quad (21)$$

$$A_1(b) = 4 \sum_{f \in b} \frac{d(f) h_0^*(f)}{S_n(f)/T} (f - f_m(b)) \quad (22)$$

are computed on the whole frequency grid, but only for the reference waveform. Also, $\langle h(f) | h(f) \rangle$ is calculated with a similar approach. In this method, the evaluation of sampled waveforms is required only to compute the bin coefficients $r_0(h, b)$ and $r_1(h, b)$ in Eq. (19). In this paper, we follow the description and implementation of Refs. [86,88]. To use relative binning with `bilby` inference, we employ the code in Ref. [89]. More details about the relative binning method applied to our analysis are given in Appendix C.

2. Simulations

We test the performance of our model in parameter estimation analysis with simulated signals. We consider three different sources, and analyze them through `bilby` injections—i.e., using our own GW models—and through injecting NR hybrids with the same parameters; cf. Table I. The employed hybrids have a postmerger signal duration of roughly 10 ms, and the postmerger contribution to their SNR for each detector network is shown in Table II.

All simulated signals are injected with zero inclination ι and polarization angle ψ , and with sky location $(\alpha, \delta) = (0.76, -1.23)$. The sky location has been chosen such that none of the employed detector networks is particularly preferred. Depending on the analysis, we perform injections at three different distances: 225 Mpc, 135 Mpc, and 68 Mpc, which, in a network with Advanced LIGO+ and Advanced Virgo+, correspond approximately to signal-to-noise ratios (SNRs) of 30, 50, and 100, respectively. Table III reports the SNRs for Source2_{QU-PM} injections in the different detector networks and at different distances. We take priors uniform in $[0.5, 1.0]$ for mass ratio q , and uniform in $[\mathcal{M}_{c,s} - 0.05, \mathcal{M}_{c,s} + 0.05] M_\odot$ for chirp mass, where $\mathcal{M}_{c,s}$ is the chirp mass of the source, and the prior width is given by the precision on chirp-mass measurements that we anticipate for future detectors. Regarding tidal deformability parameters, we sample over $\tilde{\Lambda}$ and $\Delta\tilde{\Lambda}$, with priors uniform in $[0, 5000]$ and $[-5000, 5000]$,

TABLE I. Properties of the sources used for injections. The NR hybrids are taken from the SACRA database [80], where the employed EOSs of the NR data are simple two-piece polytropes as outlined in Ref. [80]. For the hybridization, we follow the procedure outlined in Sec. III C of Ref. [13]. The inspiral waveform model with which we hybridize is SEOBNRv4T [90]. For bilby injections, we use our IMRPhenomD_NRTidalv2_Lorentzian model, both with quasiuniversal relations and with free Lorentzian parameters. In the case of injections with the free parameters model, the injected c_0 , c_1 , c_2 values are obtained from the best fit of the correspondent NR hybrid.

Name	\mathcal{M}_c	q	$\tilde{\Lambda}$	Injection
Source1 _[NR-inj]	1.17524	0.8	604	NR: H_121_151_00155 [91]
Source1 _[QU-PM]	1.17524	0.8	604	Bilby: quasiuniversal
Source1 _[FREE-PM]	1.17524	0.8	604	Bilby: free parameters
Source2 _[NR-inj]	1.08819	1.0	966	NR: H_125_125_0015 [92]
Source2 _[QU-PM]	1.08819	1.0	966	Bilby: quasiuniversal
Source2 _[FREE-PM]	1.08819	1.0	966	Bilby: free parameters
Source3 _[NR-inj]	1.17524	1.0	607	NR: H_135_135_00155 [91]
Source3 _[QU-PM]	1.17524	1.0	607	Bilby: quasiuniversal
Source3 _[FREE-PM]	1.17524	1.0	607	Bilby: free parameters

respectively, where $\Delta\tilde{\Lambda}$ is defined in Ref. [93] as

$$\Delta\tilde{\Lambda} = \frac{1}{2} \left[\sqrt{1-4\eta} \left(1 - \frac{13272}{1319}\eta + \frac{8944}{1319}\eta^2 \right) (\Lambda_1 + \Lambda_2) + \left(1 - \frac{15910}{1319}\eta + \frac{32850}{1319}\eta^2 + \frac{3380}{1319}\eta^3 \right) (\Lambda_1 - \Lambda_2) \right]. \quad (23)$$

Luminosity distance priors are uniform in comoving volume, with $D_L \in [1, 450]$ Mpc. Although all the sources considered are nonspinning, our baseline model IMRPhenomD_NRTidalv2 allows for aligned spins; we choose a uniform prior on the spin magnitudes $|\mathbf{a}_1|, |\mathbf{a}_2| \in [0.0, 0.20]$. Finally, when using the postmerger model with free parameters for recovery, we choose uniform priors $c_1 \in [2000, 4096]$ Hz and $c_2 \in [10, 200]$ Hz, while for c_0 we employ a logarithmic uniform prior in $[5 \times 10^{-27}, 1 \times 10^{-22}]$ s.

TABLE II. SNR of the NR waveforms employed in our analysis for the different detector networks (with acronyms as shown in Fig. 2), considering the source at a distance of 68 Mpc; we show both the SNR for the whole waveform (in the “Total” column), computed starting at 30 Hz, and the SNR of the postmerger part of the signal (in the “PM” column), computed starting from the merger frequency.

	Source1 _[NR-inj]		Source2 _[NR-inj]		Source3 _[NR-inj]	
	Total	PM	Total	PM	Total	PM
LHV	100	2.0	94	2.5	100	2.7
LHVKI	107	2.1	101	2.6	108	2.9
LHVKIN	126	6.8	119	8.8	126	9.9
ETCE	1267	10.2	1190	12.3	1268	13.3

D. Detector networks

Earth-based GW detectors have the best sensitivity around a few tens to hundreds of Hz, which makes the inspiral and merger signal of coalescing compact objects the perfect candidate for detections. In this work, however, we are interested in the postmerger part of the signal, which is usually weaker and involves higher frequencies. Current detectors are strongly limited at these high frequencies, but the improvements planned for the future detectors’ upgrades and the next-generation detectors are expected to make postmerger measurements feasible. Therefore, one of the goals of this work is to assess how future detectors can improve the studies we present. We include in our analysis the upgraded versions of existing detectors, Advanced LIGO+, Advanced Virgo+, and KAGRA, as well as new detectors whose construction has been planned

TABLE III. SNR values for zero-noise Source2_{QU-PM} injections in the different networks (with acronyms as shown in Fig. 2) and for different distances.

Network	Distance [Mpc]	SNR
ETCE	68	1239
	135	624
	225	355
LHVKIN	68	121
	135	61
	225	36
LHVKI	68	105
	135	53
	225	31
LHV	68	98
	135	49
	225	30

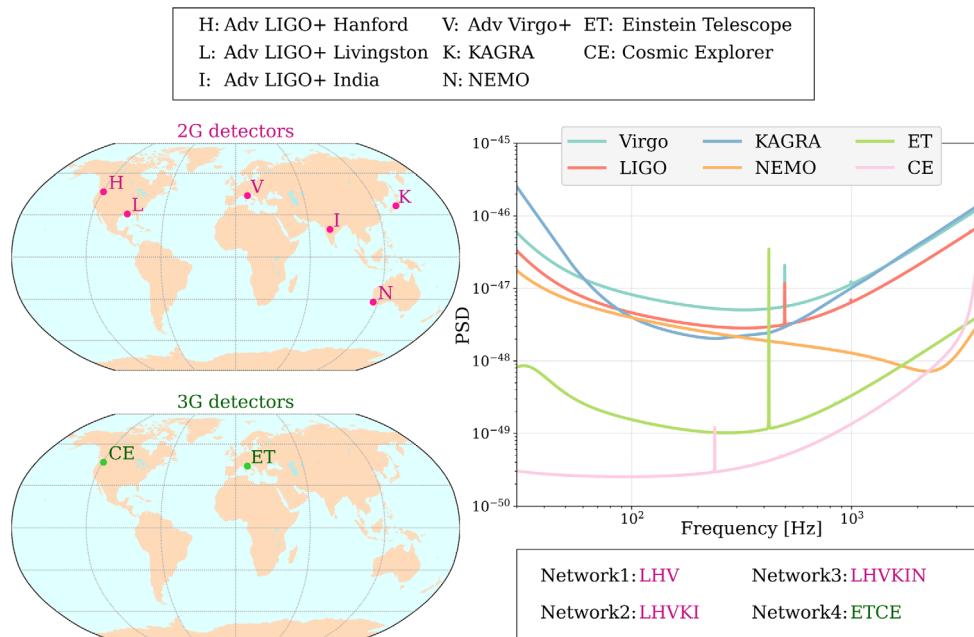


FIG. 2. *Left*: location of the detectors used in this study. The top panel shows second-generation (2G) detectors, and the bottom panel shows third-generation (3G) ones. *Right*: PSDs for the different detectors. The Advanced LIGO+ PSD [101] is used for the H, L, and I detectors. Since the official sensitivity curve for Advanced Virgo+ is not available yet, we used the same one as for the LIGO detectors, scaled by a factor $4/3$ to account for the different arm length. ET sensitivity is the PSD referred to as “ET-D” and given in Ref. [102], while CE sensitivity is given in Ref. [103]; for KAGRA, we use the PSD labeled as “Combined” in Ref. [104].

for the next few years, LIGO-India and NEMO, and the next detector generation, the Einstein Telescope and Cosmic Explorer. Advanced LIGO+ design [94] will improve the current 4 km arm-length detectors at the Hanford (H) and Livingston (L) sites, including a frequency-dependent light squeezing and new test masses with improved coating. Advanced Virgo+ (V), similarly, is the planned upgrade for the current Advanced Virgo detector in Cascina [5]. This transition will happen in two separate phases and include upgrades like the introduction of signal recycling and a higher laser power. Advanced LIGO+ and Advanced Virgo+ are the planned designs for the O5 observing run, which is scheduled to start roughly in 2025, and during which their BNS detection ranges will reach approximately 330 Mpc and 150–260 Mpc, respectively [95]. KAGRA (K) [96–98] is a 3 km arm-length interferometer built underground in the Kamioka mine in Japan, which already employs innovative technologies like cryogenic mirrors. For O5, its sensitivity at the end of the observing run is predicted to allow a BNS range of at least 130 Mpc [95]. The LIGO network involves a third detector in India (I) [99], which is currently under construction and is expected to become operative approximately in 2025. Finally, the Neutron Star Extreme Matter Observatory, or NEMO (N), is an Australian proposal for a gravitational-wave detector with 4 km arm length, specifically designed to have a high sensitivity in the kilohertz band [100]. The possible location of NEMO has not been decided yet; therefore, for this work we arbitrarily place it

at the location shown in Fig. 2. Although not officially approved yet, we include it in our analysis, since its high-frequency sensitivity is particularly interesting for post-merger studies.

3G detectors are expected to increase the sensitivity by a factor between 10 and 30 [95] with respect to current LIGO detectors, but they require the construction of new facilities and are expected to start observing in the mid 2030s. At the moment, the planned 3G detector network includes plans for Cosmic Explorer (CE) in the US and the Einstein Telescope (ET) in Europe. CE [24,25] is planned as an L-shaped interferometer with 40 km arm length.⁴ For the purpose of this paper, we assume it will be placed at the current Hanford site. The ET design [17,18] includes a so-called “xylophone” configuration, which guarantees an improved sensitivity at high and low frequencies at the same time [102]. The two candidates for the ET site are Sardinia, in Italy, and Limburg, at the border between the Netherlands, Germany, and Belgium.⁵ For this work, we assume ET is placed at the current Virgo site. Although the final design of ET is still

⁴Recently, a configuration consisting of one 40 km and an additional 20 km detector has also received attention and was considered as the reference concept for the recent Horizon study of Ref. [25]. In Ref. [105], a tunable design for the CE detector was also proposed, which would enhance sensitivity in the kilohertz band.

⁵In addition, recent interest arose for a third possible site located in the eastern part of Germany.

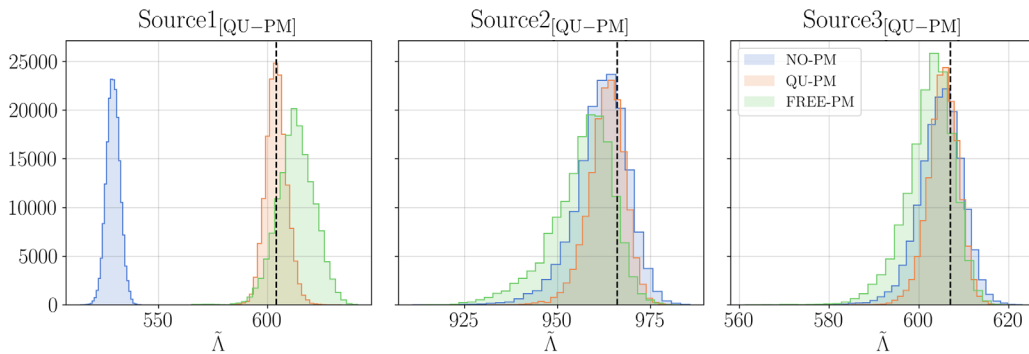


FIG. 3. Posterior probability density for $\tilde{\Lambda}$ in the case of `bilby` injections with the QU-PM model, for sources at 68 Mpc and with the ETCE network, and recovery with the three different models NO-PM, QU-PM, and FREE-PM, in blue, orange, and green, respectively. The black dashed lines correspond to the injected values.

under development, here we consider it as a triangular detector—i.e., composed of three V-shaped interferometers with a 60° opening angle and 10 km arms.

In this work, we study four different detector networks: HLV, HLVKI, HLVKIN, and ETCE. The detectors' locations and sensitivities are shown in Fig. 2.

III. RESULTS

In the following, we present the results of our simulations, for what concerns both the performance of our model and the improvement we obtain with future detectors. When using the postmerger model with quasiuniversal relations, we are mainly interested in studying how well we can recover the tidal deformability parameter $\tilde{\Lambda}$. Since the quasiuniversal relations that we derived depend on $\tilde{\Lambda}$, we expect that the postmerger part of the signal, when detected, will bring additional information about this parameter. This will likely lead to a narrower posterior with respect to what we can obtain using a model without postmerger. In the case of the postmerger model with free Lorentzian parameters, we study how well the Lorentzian parameters c_0 , c_1 , c_2 can be recovered, and especially c_1 , since it represents the frequency of the main postmerger emission peak.

A. Best-case scenario

We start by testing both versions of our model, FREE-PM and QU-PM, in the best-case scenario—i.e., for `bilby` injections in zero noise, for sources as described in Table I, at a distance of 68 Mpc and with the ETCE network. Figure 3 shows the posterior probability density of $\tilde{\Lambda}$ for signals obtained with QU-PM injections and recovered with both our postmerger models, QU-PM and FREE-PM, and with the model without postmerger NO-PM. As expected, the $\tilde{\Lambda}$ posterior becomes tighter when going from the NO-PM to the QU-PM model, with the width of the 90% confidence interval reducing by about 30%, from 23.11 to 15.84 in the case of Source2_{QU-PM}, and from 15.42 to 11.07 for Source3_{QU-PM}. In the FREE-PM

recovery case, the posteriors become wider, with the width of the 90% confidence interval reaching 27.66 for Source2_{QU-PM}. We also note that when recovering with this model, the median of $\tilde{\Lambda}$ is slightly underestimated with respect to the injected values. Both these features are predictable due to the higher number of parameters we have to sample over. For Source1_{QU-PM}, the injected value lies outside the NO-PM $\tilde{\Lambda}$ posterior distribution, but it is well recovered with both the QU-PM and FREE-PM models. Given that the sampler converged to the maximum-likelihood values for the parameters, this shift is not caused by sampling issues, but is probably due to the fact that injections are performed with a signal with postmerger, and when we recover with a model without the postmerger description, the waveform tries to latch on to the signal after the merger, causing a bias in the parameter estimation. This is confirmed by the comparison, shown in Fig. 4, between the injected Source2_{QU-PM}

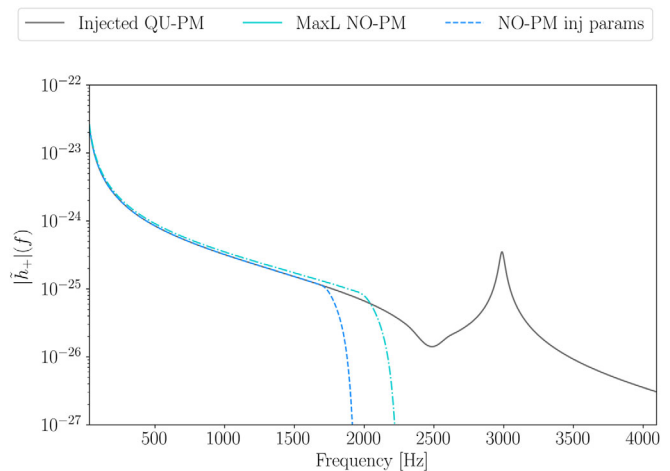


FIG. 4. Injected signal for Source1_{QU-PM} (gray solid line), compared to the NO-PM waveform generated with the injected parameters (dashed blue line) and with the maximum-likelihood parameters recovered with the NO-PM model (dash-dotted cyan line).

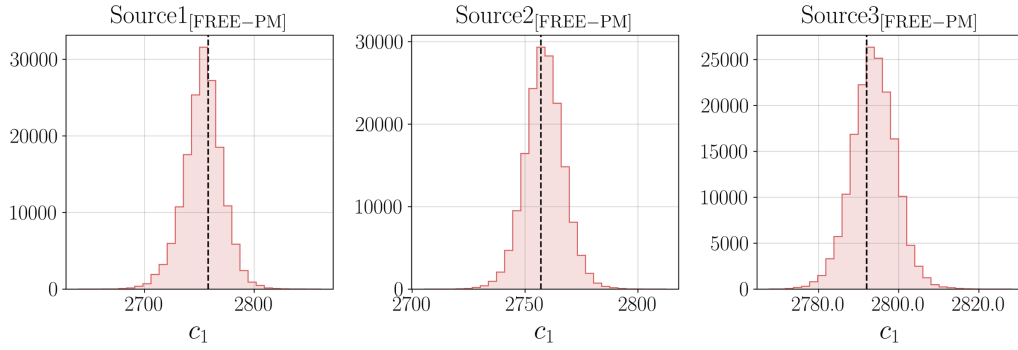


FIG. 5. Posteriors of c_1 parameters for the three different sources, obtained when using the FREE-PM model both for injection and recovery. The black dashed lines show the injected values.

waveform, the NO-PM waveform generated with the maximum-likelihood parameters recovered with the NO-PM model, and the one generated with the injected parameters. The maximum-likelihood NO-PM waveform tries to recover part of the injected postmerger signal, resulting in a deviation with respect to the NO-PM waveform obtained from the injection parameters, which explains the bias in the $\tilde{\Lambda}$ posterior.

Figure 5 shows the posteriors for the c_1 Lorentzian parameter in the case of injection and recovery with the FREE-PM model, for the three different sources. The injected values of c_0 , c_1 , c_2 are the ones that give the best fit on the NR hybrid with the same binary parameters of the source considered. The c_1 parameter, which corresponds to the frequency of the main postmerger emission peak, is well recovered in all cases. Although we are mainly interested in the recovery of c_1 , the FREE-PM model provides posteriors also for the c_0 and c_2 parameters, which are related to the maximum amplitude and width of the Lorentzian, respectively. Note that the c_0 and c_2 parameters, which are not shown in the figure, are not recovered as well as the c_1 parameter, but their injected values lie in the 90% confidence interval of the posteriors in all cases, as reported in Table IV. While our model works for our main purpose of measuring the frequency of the dominant postmerger peak, the shifts that we see in the other parameters suggest that we can further improve the FREE-PM model; see, e.g., Refs. [63,65] for recent

TABLE IV. Median with 5% and 95% quantile values of the posterior probability density for the c_0 and c_2 parameters, together with their injected values, for each of the three sources analyzed, in the case of injection and recovery with the FREE-PM model.

	$\log c_0$	$\log c_{0,\text{inj}}$	c_2	$c_{2,\text{inj}}$
Source1 _[FREE-PM]	$-56.79^{+0.29}_{-0.34}$	-56.65	$96.40^{+52.55}_{-36.90}$	74.0
Source2 _[FREE-PM]	$-56.18^{+0.21}_{-0.24}$	-56.15	$52.01^{+19.13}_{-14.19}$	48.0
Source3 _[FREE-PM]	$-55.89^{+0.19}_{-0.211}$	-55.90	$41.26^{+14.06}_{-9.52}$	39.0

developments, including postmerger features beyond the main emission frequency.

B. Detector network performances in zero noise

We want to investigate how future detector networks will improve our postmerger analysis. For this purpose, we inject signals obtained from the QU-PM model in zero noise, and we recover using both the QU-PM and the NO-PM models. We analyze signals injected at three different distances (68 Mpc, 135 Mpc, and 225 Mpc), and we compare results for the four detector networks LHV, LHVKI, LHVKIN, and ETCE (as described in Sec. II D). Due to limited computational resources, we look only at two different sources, Source2_{QU-PM} and Source3_{QU-PM}.

Figure 6 shows the Source2_{QU-PM} injected signal and the correspondent NR waveform: the signal injected with our

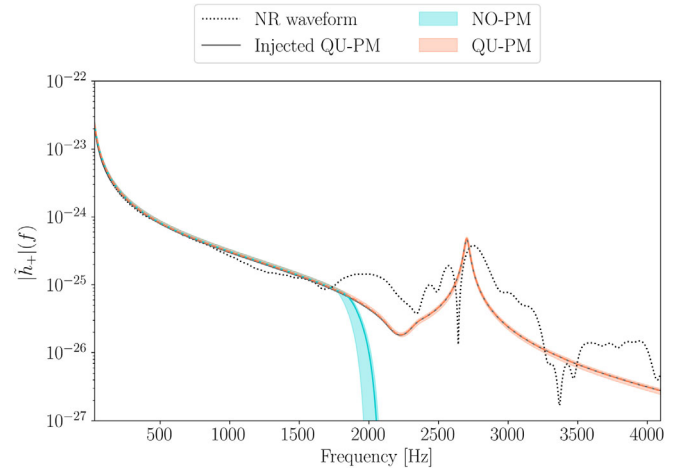


FIG. 6. Frequency domain waveform for Source2_{QU-PM}, injected at a distance of 68 Mpc and using the QU-PM model (gray solid line), and the corresponding NR waveform (black dotted line). The dashed orange line and the cyan solid line show the maximum-likelihood waveforms recovered for a zero-noise injection in the ETCE network with the QU-PM and NO-PM models, respectively. The orange and cyan shaded regions show the 90% confidence interval on the recovered waveforms for the two models.

QU-PM model describes well the main postmerger emission peak, but the NR waveform morphology also includes different subdominant emission peaks which our single Lorentzian cannot describe, and more structure in the frequency region right after the merger. Both these features should be addressed in future improvements of the model. In the same figure, we show the maximum-likelihood waveforms recovered both with the QU-PM and with the NO-PM model, for a zero-noise injection with the ETCE network. The recovered maximum-likelihood QU-PM signal overlaps with the injected one, showing how well 3G detectors will be able to recover this kind of signal. In the inspiral region, this applies also to the NO-PM maximum-likelihood waveform. The inspiral signal, which we see is well recovered also with the NO-PM model, already contains information about the $\tilde{\Lambda}$ parameter; therefore, for the ETCE network with such a high SNR, we expect that little contribution to the $\tilde{\Lambda}$ measurement comes from the postmerger part of the signal, given that this parameter is already very well constrained from the inspiral.

Figure 7 shows the uncertainty $\tilde{\Lambda}_{90\text{conf}}$, computed as the width of the 90% confidence interval of the $\tilde{\Lambda}$ posterior probability density, as a function of the detector network employed for the analysis, comparing the different distances

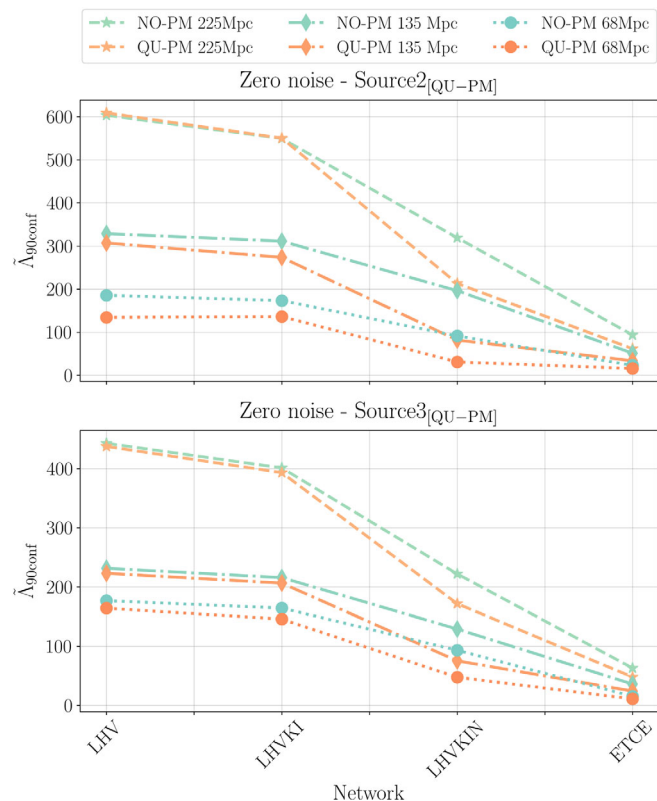


FIG. 7. Widths of the 90% confidence interval of $\tilde{\Lambda}$ posterior for Source2_{QU-PM} (top panel) and Source3_{QU-PM} (bottom panel), as functions of the different detector networks. Orange shades represent recovery with the QU-PM model; green shades represent recovery with the NO-PM one.

and recovery models. As expected, Fig. 7 shows that for all the detector networks considered, and for both models, the width of the 90% confidence interval decreases with decreasing distance. In particular, for the LHV network, we find an improvement of $\sim 50\%$ when going from 225 Mpc to 135 Mpc, and of $\sim 25\%$ (for Source2_{QU-PM}, even 56%) when going from 135 Mpc to 68 Mpc, for both models; for the ETCE network, we find an improvement of $\sim 45\%$ when going from 225 Mpc to 135 Mpc, and of $\sim 55\%$ when going from 135 Mpc to 68 Mpc. Using the QU-PM model yields systematically tighter constraints on $\tilde{\Lambda}$, thanks to the additional information arising from the quasiuniversal relations that describe the postmerger part of the signal. For both the sources, in the case of injections at 225 Mpc and with the LHV or LHVKI network, we see no significant differences in $\tilde{\Lambda}_{90\text{conf}}$ in the case of recovery with the QU-PM or NO-PM model. Considering that such injections generate a $\text{SNR} \simeq 30$ in the case of the LHV network, this is consistent with the fact that in these situations, we do not detect the postmerger signal.

Interestingly, the best improvement when using the QU-PM model comes in the case of the LHVKIN network. Going from the LHVKIN to the ETCE network, the constraint on $\tilde{\Lambda}$ improves by about $\sim 70\%$ for both models, while adding NEMO to the LHVKI network leads to an improvement in $\tilde{\Lambda}_{90\text{conf}}$ of $\sim 60\%$ for the QU-PM model, against just $\sim 40\%$ for the NO-PM model. For both sources, we also see that for the LHVKIN network, the constraint on $\tilde{\Lambda}$ obtained with the QU-PM model for injections at 135 Mpc is better than the one we retrieve with the NO-PM model for injections at 68 Mpc. 3G detectors are expected to have the best sensitivity over the whole frequency band, and indeed we see that for the ETCE network we get the smallest $\tilde{\Lambda}_{90\text{conf}}$ for both models. However, the high sensitivity at lower frequencies allows us to obtain precise measurements of $\tilde{\Lambda}$ from the inspiral part of the signal alone, therefore reducing the impact of the possible information gained from the postmerger phase. In the case of the LHVKIN network, instead, the constraint on $\tilde{\Lambda}$ from the inspiral is that of second-generation detectors, but the high sensitivity of NEMO in the kilohertz band leads to a better detection of the postmerger, and therefore to significantly tighter constraints when using the QU-PM model. If its realization is approved, adding NEMO to the network of second-generation detectors will significantly help the detection of postmerger signals and related studies. We note that for this work, we analyze signals with a lower-frequency cutoff of $f_{\text{low}} = 30$ Hz, missing many inspiral cycles; in reality, an additional improvement on $\tilde{\Lambda}$ measurements will be provided by the use of a lower f_{low} .

C. Detector network performances in nonzero noise

In the previous sections, we focused on model and network performances, using injections in zero noise. Now, we want to look at the influence of noise on our

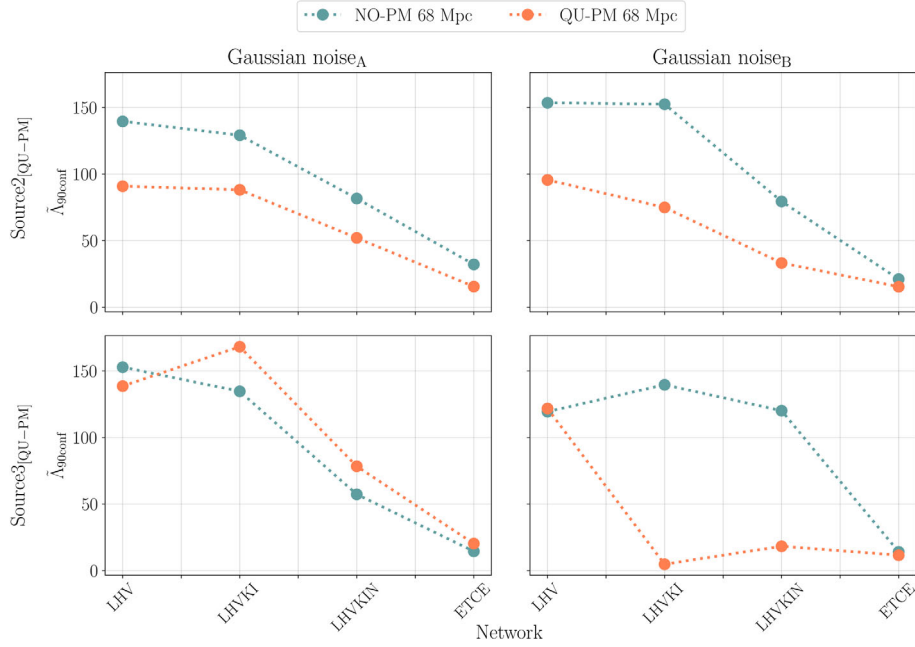


FIG. 8. Width of the 90% confidence interval of the $\tilde{\Lambda}$ posterior for Source2_{QU-PM} (top row) and Source3_{QU-PM} (bottom row), as a function of the different detector networks, obtained with two different noise realizations: noise_A for the left panels, and noise_B for the right ones.

study. For this reason, we repeat the analysis using Gaussian noise. Due to limited computational resources, we restrict our focus to only two sources, Source2_{QU-PM} and Source3_{QU-PM}, and to one distance, 68 Mpc. We inject signals using the QU-PM model, and we recover them with both the QU-PM and NO-PM models, comparing results for the different detector networks LHV, LHVKI, LHVKIN, and ETCE. Figure 8 shows $\tilde{\Lambda}_{90\text{conf}}$ for the different detector networks. In order to assess the impact of noise fluctuations, we show results for two different noise realizations, which we call noise_A and noise_B. Due to the noise impact on the analysis, we do not see the clear trends that we found in the zero-noise runs, as described in Sec. III B. In the case of Source3_{QU-PM} (bottom panels in Fig. 8), with the noise_A realization, the constraints obtained with the QU-PM model are even wider than the ones recovered with the NO-PM model. The most extreme fluctuation is found for Source3_{QU-PM}, in the case of LHVKI network and QU-PM model, for which $\tilde{\Lambda}_{90\text{conf}} = 88.26$ in the case of noise_A and $\tilde{\Lambda}_{90\text{conf}} = 4.84$ for noise_B. However, we see that in general, $\tilde{\Lambda}_{90\text{conf}}$ decreases with more advanced detectors, with an improvement between 80% and 90% when going from the LHV to the ETCE network. In most cases, the QU-PM model allows us to better determine $\tilde{\Lambda}$, although the quantitative improvement strongly depends on the source and especially on the noise realization. Moreover, noise fluctuations also impact the median of the $\tilde{\Lambda}$ posterior probability density, causing different shifts with respect to the injected values (see Table V). Although such shifts appear to be small, they can cause the posterior's median to lie outside the 90% confidence

interval, especially in the case of the ETCE network, where the $\tilde{\Lambda}_{90\text{conf}}$ is indeed very small.

D. Numerical relativity injections

Finally, we analyze simulated signals obtained by injecting NR waveforms on top of Gaussian noise. Figure 9 shows the posterior probability density of $\tilde{\Lambda}$ for injections at 68 Mpc in the ETCE network. For Source2_[NR-inj], the recovered posteriors of $\tilde{\Lambda}$ peak at the injected value, but for the other sources, the posterior is shifted with respect to it. For Source1_{QU-PM}, the $\tilde{\Lambda}$ injected value lies in the tail of the posteriors recovered with the QU-PM and FREE-PM models, and completely outside the posterior obtained with the NO-PM model; for Source3_{QU-PM}, the posteriors recovered with all the models peak at values between 575 and 578,

TABLE V. Median values with 90% confidence interval for the posterior probability density of $\tilde{\Lambda}$ in the case of two different noise realizations, labeled as noise_A and noise_B, for injections at 68 Mpc in the ETCE network and for recovery with the two different models QU-PM and NO-PM; the last column reports the injected value of $\tilde{\Lambda}$.

	Model	$\tilde{\Lambda}_m$ noise _A	$\tilde{\Lambda}_m$ noise _B	$\tilde{\Lambda}_{\text{inj}}$
Source2 _{QU-PM}	QU-PM	956.68 ^{+7.08} _{-8.37}	959.93 ^{+6.87} _{-8.71}	966
	NO-PM	966.35 ^{+9.35} _{-11.82}	953.10 ^{+13.11} _{-19.11}	966
Source3 _{QU-PM}	QU-PM	608.04 ^{+11.65} _{-6.27}	602.36 ^{+7.86} _{-12.49}	607
	NO-PM	611.76 ^{+6.68} _{-7.51}	604.35 ^{+6.84} _{-7.70}	607

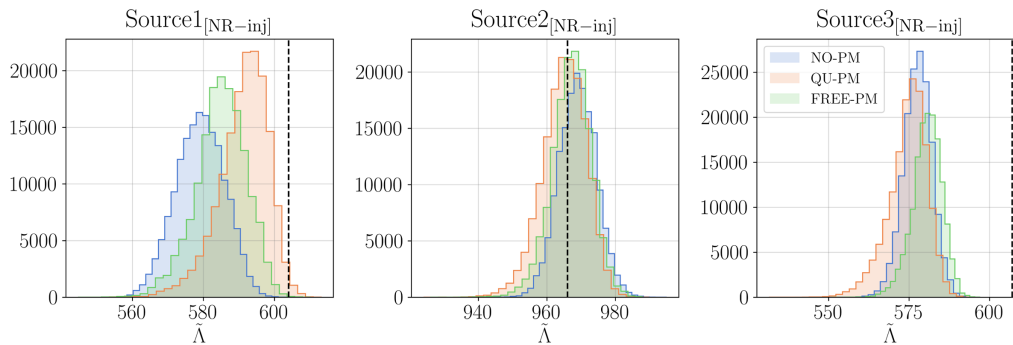


FIG. 9. Posterior probability density for $\tilde{\Lambda}$ as recovered with different models (NO-PM, QU-PM, and FREE-PM) in the case of signals simulated by injecting NR waveforms into Gaussian noise at a distance of 68 Mpc, for the ETCE detector networks. The black dashed lines show the injected values.

with the injected value $\tilde{\Lambda} = 607$ lying completely outside their distributions. These shifts are due to noise fluctuations, as we showed in Sec. III C, and possible limitations of our waveform models. The case analyzed here, using the ETCE network, generates a signal with a high SNR, and therefore a narrow posterior density for $\tilde{\Lambda}$; hence, the shifts induced by noise fluctuations can result in the injected value being situated outside the 90% confidence interval. Using one of the postmerger models to analyze signals obtained with NR waveforms does not lead to a meaningful improvement in the $\tilde{\Lambda}$ constraints like the ones shown in Sec. III A. This is consistent with the fact that mismatches computed over the whole waveform (cf. lower panel of Fig. 1) do not show significant improvements when using one of the postmerger models, considering that the noise and the complicated morphology of the NR injection make it more difficult for our models to recover the postmerger part of the signal, and therefore almost all the $\tilde{\Lambda}$ information comes from the inspiral phase. Nonetheless, when using the postmerger models, we see a modest improvement in the recovery of $\tilde{\Lambda}$ for Source2_[NR-inj] with respect to the NO-PM one, and a clear improvement for Source1_[NR-inj]. The latter is consistent with the results found in Sec. III A for Source1_{QU-PM}, where we concluded that, when using the NO-PM model, the presence of a postmerger signal, to which the NO-PM waveform tries to latch on, causes a bias in the $\tilde{\Lambda}$ parameter recovery. In Sec. III C, we saw that noise fluctuations alone can impact the performance of our model, but in this case an additional issue is that the NR simulations contain a more complex GW structure in the postmerger phase, which is not fully recovered with our simple Lorentzian model. This appears clearly in Fig. 10, which shows the injected NR waveform together with the maximum-likelihood ones recovered with the different models and their 90% confidence interval. The postmerger peak obtained with the QU-PM model is slightly shifted with respect to the main postmerger peak of the NR waveform; however, the same shift was present also in the Source2_{QU-PM} injected waveform in Fig. 6, and hence we conclude that it is due to the

imperfection of the model, not to issues in the parameter estimation process. When optimizing the mismatches to compute the best values of the fit parameters for our quasiuniversal relations, it is likely that the model tries to adapt to the whole morphology of the postmerger NR signal, thus shifting with respect to what would be the description of the main emission peak only. For the FREE-PM model maximum-likelihood waveform, the postmerger peak lies at a higher frequency than the true one, is much wider, and has a nonphysical amplitude, though this does not affect the $\tilde{\Lambda}$ recovery (cf. Fig. 9). Given the large bias in c_0 , and the fact that the injected values vary in a small range, an improvement would probably be obtained already by restricting the prior range for this parameter. For comparison, in Fig. 10, we show also the waveform obtained from the FREE-PM model with the optimized parameters computed as explained in

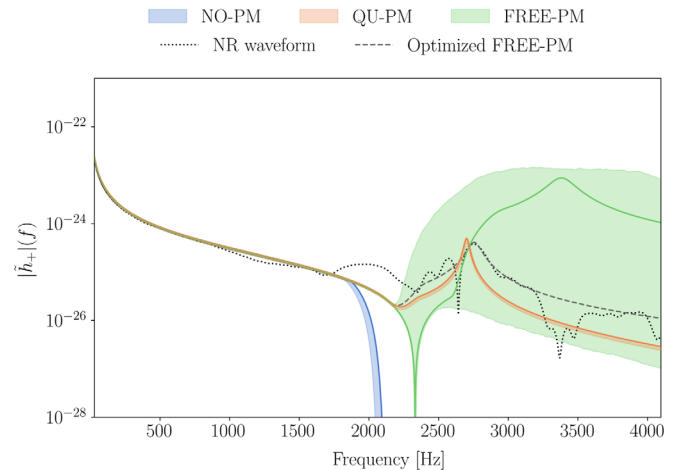


FIG. 10. Frequency-domain waveform of the injected NR (black dotted line) waveform, compared to the waveforms generated from the maximum-likelihood parameters recovered for each model. The dashed gray line shows the FREE-PM waveform obtained by optimizing the Lorentzian parameters as explained in Sec. II B. The shaded regions represent the 90% confidence interval of the posterior of the recovered waveform with the different models.

Sec. II B: the postmerger peak of the optimized FREE-PM waveform overlaps to that of the NR waveform. Hence, the FREE-PM model can in principle describe the data well, but the additional information contained in the complex and more structured morphology of the postmerger in the hybrid signal makes it challenging for our simple model to recover all the parameters correctly. The fact that the postmerger Lorentzian parameters cannot be recovered with good precision causes the 90% confidence interval of the recovered waveform to be very broad. The spectra recovered with the QU-PM model, instead, lie in a narrower interval because their values are determined by the binary’s parameters, which with 3G detectors are recovered with a very high precision (see Appendix B). We also note that the optimized FREE-PM model peak does not present the same shift as the QU-PM one, which is consistent with the fact that the mismatches in the high-frequency region shown in Fig. 1 are systematically lower for the FREE-PM model. For this purpose, both our QU-PM and FREE-PM models need to be improved toward more structured signals. Moreover, hybridization of NR waveforms starts from the last few cycles of the inspiral, so that the late-inspiral and merger waveform is also based on NR simulations, and is thus different from the model we employ. The difference between the hybrids and the waveform models in the late-inspiral region is visible also in Fig. 10 and can lead to biases, affecting the results obtained not only with our FREE-PM or QU-PM models, but also with the model without postmerger.

IV. CONCLUSIONS

We have developed an analytical, frequency-domain model to describe the GW emission during the inspiral, merger, and postmerger phases of a BNS coalescence. For the inspiral and merger phases, we employed the `IMRPhenomD_NRTidalv2` waveform. We incorporate the postmerger part through modeling the main emission peak with a Lorentzian, whose parameters, in the two versions of our model, are either free or determined by quasiuniversal relations. Due to the computational cost of the analysis, our study was limited to a restricted number of BNS systems. We have shown that in the best-case scenario of simulations with zero noise and high SNR—i.e., at a distance of 68 Mpc and with the ETCE network—the QU-PM model leads to better constraints on the $\tilde{\Lambda}$ posteriors compared to the ones obtained with the NO-PM model, and the FREE-PM model grants an accurate measurement of the frequency of the main postmerger emission peak. Within our study, we find that noise fluctuations can significantly impact the results; as shown in Sec. III C, they produce both large differences in the accuracy of $\tilde{\Lambda}$ measurements (quantified by the width of the 90% confidence interval of the recovered $\tilde{\Lambda}$ posterior; e.g., Fig. 8), and shifts in the median value of that posterior, cf. Table V. In some cases, this overcomes the improvement

on $\tilde{\Lambda}$ measurements yielded by the use of the QU-PM model and calls for caution in the interpretation of the results, to distinguish the effects of a different model from the effects of noise. It is important to note that the shifts in $\tilde{\Lambda}$ recovery caused by noise fluctuations, which are evident especially in high-SNR injections, given the narrowing of the posterior, also affect the results obtained using the model without postmerger. In general, including the postmerger during the analysis provides tighter constraints on the $\tilde{\Lambda}$ posterior than the original inspiral-only `IMRPhenomD_NRTidalv2` model. Finally, we used our model to recover signals obtained by injecting NR waveforms. Although we still see improvements in some cases when using the postmerger models, they are not as significant as those we found for the simulated signals. This is due to noise effects and the fact that NR waveforms include postmerger signals with a complex structure, which a simple Lorentzian model struggles to recover. Despite the promising results, we conclude that our model, in both its versions, still needs improvements in order to be employed in the analysis of real signals.

Another central point of our study was to assess the performance of different detector networks, and to understand how future detectors will improve the postmerger analysis. In particular, we considered four different networks: (i) advanced LIGO+ in Hanford and Livingston together with Advanced Virgo+; (ii) the same network as (i) extended by KAGRA and LIGO-India; (iii) the same network as (ii) extended with NEMO; and (iv) a network consisting of a 40 km Cosmic Explorer and a 10 km, triangular Einstein Telescope. Although 3G detectors, as expected, will give the best constraints on $\tilde{\Lambda}$, we found that NEMO, thanks to its very high sensitivity in the kilohertz band, yields the biggest improvement when using the QU-PM model.

Our study showed how, with future detector networks, GW observations from the postmerger phase of a BNS coalescence will allow us to unravel information about the fundamental physics describing supranuclear-dense matter.

ACKNOWLEDGMENTS

We thank Anuradha Samajdar for the useful discussion. A. P., C. K., Y. S., and C. V. D. B. are supported by the research program of the Netherlands Organisation for Scientific Research (NWO). This work was performed using the Computing Infrastructure of Nikhef, which is part of the research program of the Foundation for Nederlandse Wetenschappelijk Onderzoek Instituten (NWO-I), which is part of the Dutch Research Council (NWO). The authors are grateful for computational resources provided by the LIGO Laboratory and supported by National Science Foundation Grants No. PHY-0757058 and No. PHY-0823459. This research has made use of data, software, and/or web tools obtained from the Gravitational Wave Open Science

Center [106], a service of LIGO Laboratory, the LIGO Scientific Collaboration, and the Virgo Collaboration. LIGO is funded by the U.S. National Science Foundation. Virgo is funded by the French Centre National de Recherche Scientifique (CNRS), the Italian Istituto Nazionale della Fisica Nucleare (INFN), and the Dutch Nikhef, with contributions by Polish and Hungarian institutes.

APPENDIX A: RESULTS FOR THE FREE-PARAMETER MODEL

In the following, we show some results obtained with the postmerger model using free Lorentzian parameters. Performing parameter estimation analysis with the FREE-PM waveform requires sampling over three additional parameters, which implies even higher computational costs. For this reason, we could not run the same analyses with the FREE-PM model as we did for the QU-PM one. As shown in Sec. III A, with high-SNR and zero-noise injections, we can recover c_1 accurately. In Fig. 11, we show how different detector networks can recover the c_1 parameter in the case of Gaussian noise injections, for simulated signals corresponding to Source3_{FREE-PM} at 68 Mpc. In the case of second-generation detectors, we basically recover the prior, although with a peak within [2500,3000] Hz, where the injected value also lies. Adding NEMO to the network leads to a strong improvement, resulting in a very sharp peak for the c_1 posterior. The recovered value of c_1 with the LHVKIN network is slightly overestimated with respect to the injected value. However, this happens also for the ETCE network, where again the posterior is a sharp peak, and the injected value lies in its lower tail, outside of the 90% confidence interval. In Sec. III A, we saw that, for the ETCE network, for the same simulated signal injected in zero noise, the value of c_1 is recovered very well. Therefore, we conclude that the

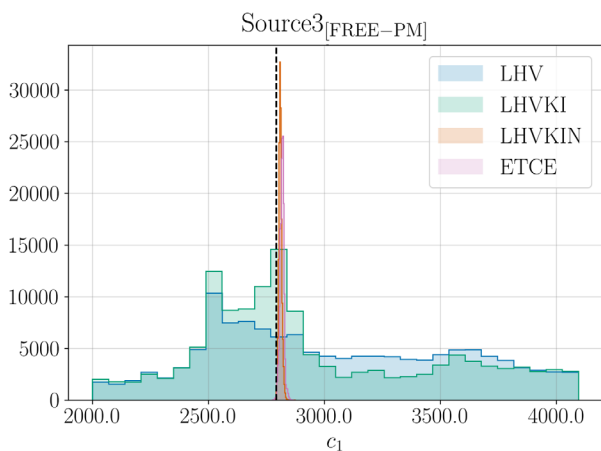


FIG. 11. Posterior probability density for the c_1 Lorentzian parameter for the different detector networks, in the case of Gaussian noise injections at 68 Mpc. The dashed vertical line indicates the injected value.

shifts in the posterior peaks for the ETCE and LHVKIN networks for the injections in Gaussian noise are most likely due to noise fluctuations, which, as reported in Sec. III C, for this source affect also the $\tilde{\Lambda}$ measurements. Finally, analyses of signals obtained by NR waveform injections do not recover either of the Lorentzian parameters, mainly because of the complex structure of the postmerger signal in the NR waveforms, as already shown in Sec. III D. Although the FREE-PM model still needs improvement for the analysis of real signals, the results in Fig. 11 are promising, and especially show that adding NEMO to a network of second-generation detectors will certainly make a difference for the study of BNS postmerger signals.

APPENDIX B: PARAMETER ESTIMATION WITH FUTURE DETECTORS

Our discussion focused on the recovery of the $\tilde{\Lambda}$ parameter, or of the c_1 parameter in the case of the FREE-PM model, because these are the quantities that encode most of the information about the EOS. However, it is also interesting to look at the recovery of all the other binary parameters, to see how future detectors will help in improving our knowledge of these systems. Figure 12 shows the comparison between the normalized posterior probability density for \mathcal{M}_c , q , $\tilde{\Lambda}$, χ_1 , χ_2 , α , δ and luminosity distance d_L , obtained using different detector networks, for Source2_{QU-PM} injections at 68 Mpc and in zero noise. We find that 3G detectors will yield a strong improvement not only for what concerns $\tilde{\Lambda}$ recovery, but also in the estimation of \mathcal{M}_c , q , and d_L ; in particular, with the ETCE network we can estimate \mathcal{M}_c with a precision roughly 10 times better than the LHV one. We find only a slight improvement in the recovery of the spin magnitude values χ_1 and χ_2 . The best estimation of the sky location parameters (α , δ) comes from the LHVKIN network, which is expected, considering the larger number of detectors and their geographical distribution, as shown in Fig. 2. We also note that the improvement obtained by adding NEMO to the network is roughly a factor of 1.9 and 1.6 for \mathcal{M}_c and q , respectively, when computed in comparison with the LHVKI network, but it reaches a factor of 4.4 for $\tilde{\Lambda}$ estimation. As discussed in Sec. III B, this is achieved thanks to the postmerger contribution to the signal, which for NEMO is significant as a result of its very high sensitivity in the kilohertz band. Overall, future detectors will grant very precise constraints on the BNS parameters, allowing us to better understand the properties and populations of these objects. We also point out that, for computational reasons, our analyses were performed starting from a frequency $f_{\text{low}} = 30$ Hz, and hence, in reality, additional information will be available by analyzing signals starting from lower frequencies. This will lead to a large improvement, especially for the 3G detectors,

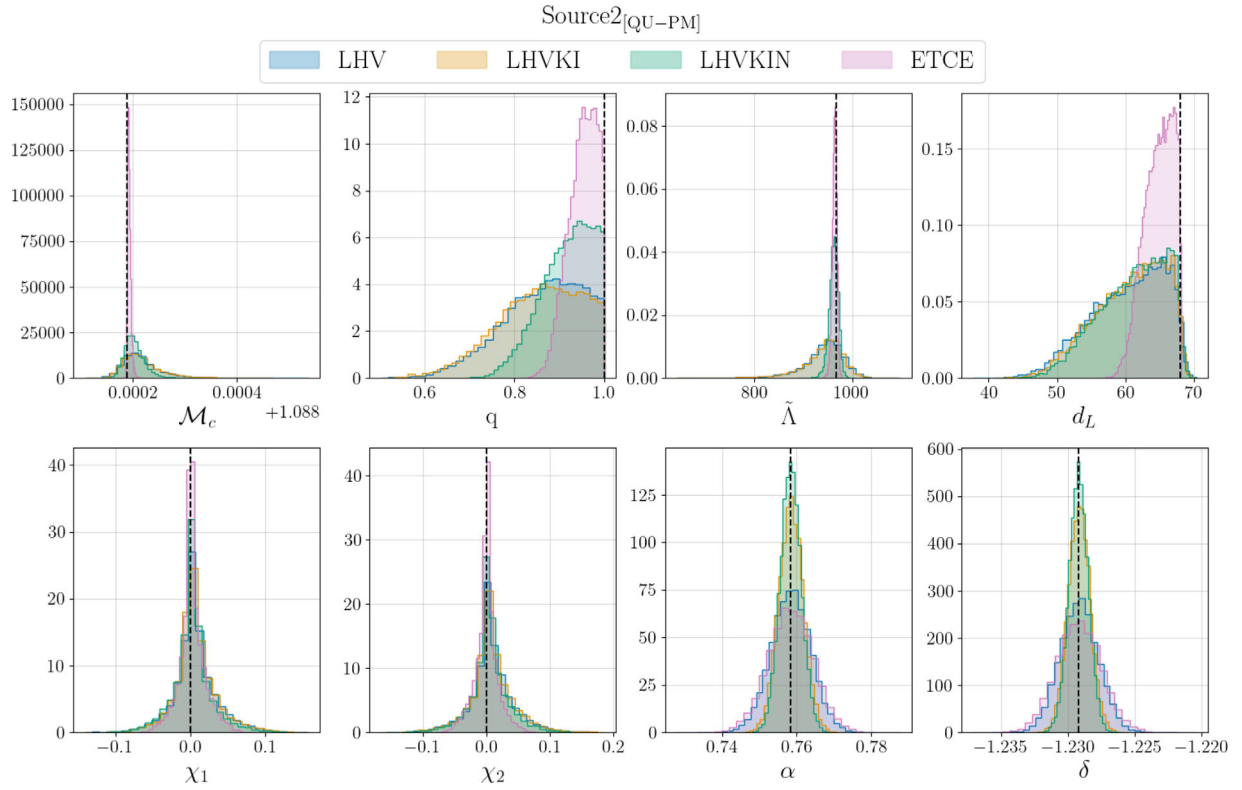


FIG. 12. Normalized posterior probability density for the binary parameters recovered with the QU-PM model with the different detector networks, for Source2_{QU-PM} at 68 Mpc; the dashed vertical lines show the injected values.

because, for example, the xylophone configuration of ET, with the low-frequency interferometer possibly operating at cryogenic temperatures, will ensure a good sensitivity down to $f_{\text{low}} = 5$ Hz. The additional information carried in the many inspiral cycles at low frequencies will further improve the constraints on the BNS parameters, being particularly beneficial for the spin parameters, considering that at low frequencies, spin-induced quadrupole moment effects also become significant.

APPENDIX C: RELATIVE BINNING SETTINGS AND VALIDITY

The relative binning method allows us to greatly reduce the computational cost of our analysis. As explained in Sec. II C 1, a fundamental requirement to employ this technique is having a reference waveform that describes the data sufficiently well. Although with real data we do not know the exact parameters of the source *a priori*, we can use information from low-latency analyses and quasiuniversal relations to find the values to use as the fiducial parameters. Since there might still be biases in the parameters determined in such a way, we checked the influence of the choice of fiducial parameters, performing some tests with different fiducial values for Λ_1, Λ_2 , and we found consistency between results.

In Ref. [86], the authors show results obtained with this method for GW170817, which, despite being a loud event, has a SNR much lower than the ones we study in this work (cf. Table III). The approximations used in relative binning are not expected to retain validity only in a given SNR range, but we tested the efficacy of this method applied to very loud signals by checking the consistency against results obtained with the nested sampling package LALINFERENCE [107] of the LIGO Algorithms Library (LAL) software suite [108].

Finally, when using the relative binning method, the choice of frequency bins in which the waveform is evaluated plays a crucial role. Following Ref. [86], this choice is dictated by the requirement that the differential phase change in each bin be smaller than some threshold δ_ϕ . In Ref. [86], the phase change is computed assuming a post-Newtonian (PN) description of the signal, in which the effects of the different binary parameters enter the phase with different powers of frequency. In the merger and postmerger part of the signal, the PN approximation is not valid anymore. It is not easy to find a similar way to properly describe the phase in the postmerger without having to evaluate the waveform and incurring computationally expensive processes that would undermine the speedup advantage of this method. On the other hand, the phase computed with the PN approximation is then interpolated with frequency, and the frequency bins are

TABLE VI. Number of frequency bins employed in the relative binning method for different values of δ_ϕ , both for the frequency range [30, 4096] Hz and in the postmerger region, starting at the merger frequency.

δ_ϕ	Total bins	PM bins
0.005	6285	2767
0.007	4489	1976
0.01	3143	1384
0.03	1049	462
0.05	630	277

determined by evaluating this interpolant over a grid of phases determined by the required precision δ_ϕ . Therefore, if such a threshold is chosen to be small enough (for our analysis, we set $\delta_\phi = 0.01$), we expect that the way in which the phase change is computed will play little role, and the dense frequency binning produced ensures that the bins' widths will be small enough to allow a linear interpolation of the ratio between the generated waveform and the fiducial one anyway, as in Eq. (19). If this were not true, we would expect that changing the threshold δ_ϕ , and consequently the frequency bins, over which the waveform is evaluated

would give different results also if δ_ϕ were kept small. Table VI reports the number of frequency bins employed by the relative binning technique for different values of δ_ϕ , both in the whole frequency range considered for the analysis, and for the postmerger region only. Choosing small values of δ_ϕ means increasing the number of bins over which we evaluate the waveform, and therefore the computational cost of the analysis; nevertheless, performing the analysis using relative binning with these settings is still much faster than running “standard” parameter estimation analyses, which, for these kinds of signals, are not computationally feasible. For standard parameter estimation, the waveform needs to be evaluated on a uniform grid that, with signals of a duration of roughly 200 s such as the ones analyzed here, includes approximately 8×10^4 points. Hence, considering that relative binning needs the evaluation of each sampled waveform only at the edges of the bins, this technique greatly reduces the number of required waveform evaluations. Figure 13 shows the posteriors recovered with the QU-PM model for the binary parameters of a Source2_{QU-PM} injection at 135 Mpc, with the LHVKIN network. We repeated the analysis multiple times, keeping the same settings but changing the frequency binning by using different values of δ_ϕ . We keep δ_ϕ small, but we look at

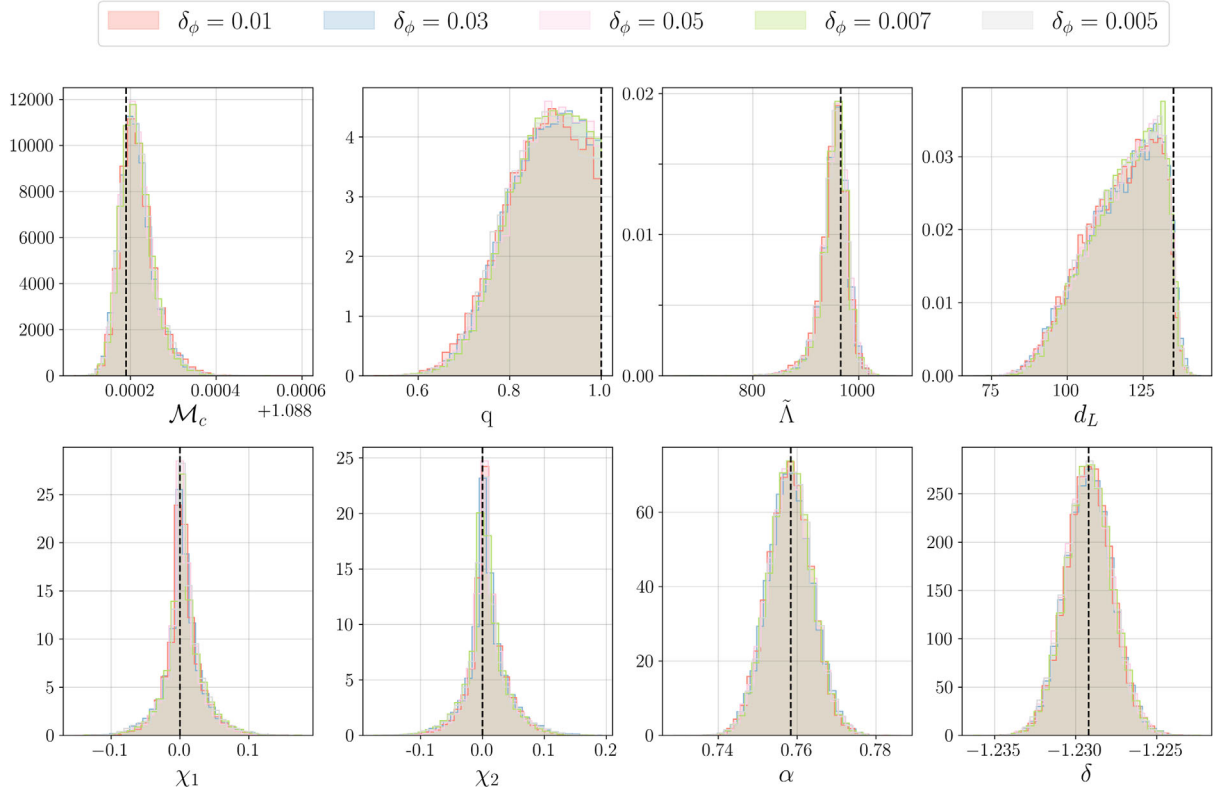


FIG. 13. Comparison between the normalized posteriors for the binary parameters recovered with the QU-PM model for Source2_{QU-PM} injections at 135 Mpc with the LHVKIN network, using the relative binning technique with different precision requirements. The different colors show the posteriors for the analysis with different values of δ_ϕ , while the black dashed lines represent the injected values.

both larger and smaller values with respect to the $\delta_\phi = 0.01$ used throughout this work. As the plot shows, we find great consistency between the results obtained with all the different values of δ_ϕ . Consequently, despite the fact that

the PN approximation does not hold in the postmerger phase, using it to determine the frequency bins for the relative binning method does not spoil the results, provided that the chosen δ_ϕ results in small bin widths.

-
- [1] B. P. Abbott *et al.* (LIGO Scientific, Virgo Collaborations), *Phys. Rev. Lett.* **119**, 161101 (2017).
- [2] T. Dietrich, T. Hinderer, and A. Samajdar, *Gen. Relativ. Gravit.* **53**, 27 (2021).
- [3] K. Chatziioannou, *Gen. Relativ. Gravit.* **52**, 109 (2020).
- [4] J. Aasi *et al.* (LIGO Scientific Collaboration), *Classical Quantum Gravity* **32**, 074001 (2015).
- [5] F. Acernese *et al.* (Virgo Collaboration), *Classical Quantum Gravity* **32**, 024001 (2015).
- [6] B. P. Abbott *et al.* (LIGO Scientific, Virgo Collaborations), *Phys. Rev. X* **9**, 011001 (2019).
- [7] B. P. Abbott *et al.* (LIGO Scientific, Virgo Collaborations), *Astrophys. J. Lett.* **892**, L3 (2020).
- [8] T. Hinderer, B. D. Lackey, R. N. Lang, and J. S. Read, *Phys. Rev. D* **81**, 123016 (2010).
- [9] T. Damour, A. Nagar, and L. Villain, *Phys. Rev. D* **85**, 123007 (2012).
- [10] W. Del Pozzo, T. G. F. Li, M. Agathos, C. Van Den Broeck, and S. Vitale, *Phys. Rev. Lett.* **111**, 071101 (2013).
- [11] B. D. Lackey and L. Wade, *Phys. Rev. D* **91**, 043002 (2015).
- [12] M. Agathos, J. Meidam, W. Del Pozzo, T. G. F. Li, M. Tompitak, J. Veitch, S. Vitale, and C. Van Den Broeck, *Phys. Rev. D* **92**, 023012 (2015).
- [13] T. Dietrich *et al.*, *Phys. Rev. D* **99**, 024029 (2019).
- [14] K. Kawaguchi, K. Kiuchi, K. Kyutoku, Y. Sekiguchi, M. Shibata, and K. Taniguchi, *Phys. Rev. D* **97**, 044044 (2018).
- [15] T. Hinderer, *Astrophys. J.* **677**, 1216 (2008).
- [16] T. Damour and A. Nagar, *Phys. Rev. D* **81**, 084016 (2010).
- [17] M. Punturo *et al.*, *Classical Quantum Gravity* **27**, 194002 (2010).
- [18] M. Maggiore *et al.*, *J. Cosmol. Astropart. Phys.* **03** (2020) 050.
- [19] A. Freise, S. Chelkowski, S. Hild, W. Del Pozzo, A. Perreca, and A. Vecchio, *Classical Quantum Gravity* **26**, 085012 (2009).
- [20] S. Hild, S. Chelkowski, A. Freise, J. Franc, N. Morgado, R. Flaminio, and R. DeSalvo, *Classical Quantum Gravity* **27**, 015003 (2010).
- [21] B. Sathyaprakash *et al.*, in *46th Rencontres de Moriond on Gravitational Waves and Experimental Gravity* (2011), pp. 127–136, [arXiv:1108.1423](https://arxiv.org/abs/1108.1423).
- [22] C. Pacilio, A. Maselli, M. Fasano, and P. Pani, *Phys. Rev. Lett.* **128**, 101101 (2022).
- [23] P. K. Gupta, A. Puecher, P. T. H. Pang, J. Janquart, G. Koekoek, and C. Broeck Van Den, [arXiv:2205.01182](https://arxiv.org/abs/2205.01182).
- [24] D. Reitze *et al.*, [arXiv:1907.04833](https://arxiv.org/abs/1907.04833).
- [25] M. Evans *et al.*, [arXiv:2109.09882](https://arxiv.org/abs/2109.09882).
- [26] S. Köppel, L. Bovard, and L. Rezzolla, *Astrophys. J.* **872**, L16 (2019).
- [27] A. Bauswein, T. W. Baumgarte, and H. T. Janka, *Phys. Rev. Lett.* **111**, 131101 (2013).
- [28] L. Baiotti, B. Giacomazzo, and L. Rezzolla, *Phys. Rev. D* **78**, 084033 (2008).
- [29] S. Bernuzzi, *Gen. Relativ. Gravit.* **52**, 108 (2020).
- [30] L. Baiotti and L. Rezzolla, *Rep. Prog. Phys.* **80**, 096901 (2017).
- [31] P. T. H. Pang *et al.*, [arXiv:2205.08513](https://arxiv.org/abs/2205.08513).
- [32] P. Hammond, I. Hawke, and N. Andersson, *Phys. Rev. D* **104**, 103006 (2021).
- [33] C. Raithel, V. Paschalidis, and F. Özel, *Phys. Rev. D* **104**, 063016 (2021).
- [34] E. R. Most, A. Haber, S. P. Harris, Z. Zhang, M. G. Alford, and J. Noronha, [arXiv:2207.00442](https://arxiv.org/abs/2207.00442).
- [35] W. Kastaun and F. Galeazzi, *Phys. Rev. D* **91**, 064027 (2015).
- [36] A. Bauswein, H. T. Janka, K. Hebeler, and A. Schwenk, *Phys. Rev. D* **86**, 063001 (2012).
- [37] K. Takami, L. Rezzolla, and L. Baiotti, *Phys. Rev. D* **91**, 064001 (2015).
- [38] S. Bernuzzi, T. Dietrich, and A. Nagar, *Phys. Rev. Lett.* **115**, 091101 (2015).
- [39] A. Bauswein and N. Stergioulas, *Phys. Rev. D* **91**, 124056 (2015).
- [40] B. P. Abbott *et al.* (LIGO Scientific, Virgo Collaborations), *Astrophys. J. Lett.* **851**, L16 (2017).
- [41] B. P. Abbott *et al.* (LIGO Scientific, Virgo Collaborations), *Astrophys. J.* **875**, 160 (2019).
- [42] A. Bauswein, N.-U. F. Bastian, D. B. Blaschke, K. Chatziioannou, J. A. Clark, T. Fischer, and M. Oertel, *Phys. Rev. Lett.* **122**, 061102 (2019).
- [43] E. R. Most, L. J. Papenfort, V. Dexheimer, M. Hanauske, S. Schramm, H. Stöcker, and L. Rezzolla, *Phys. Rev. Lett.* **122**, 061101 (2019).
- [44] D. M. Siegel, R. Ciolfi, A. I. Harte, and L. Rezzolla, *Phys. Rev. D* **87**, 121302 (2013).
- [45] M. G. Alford, L. Bovard, M. Hanauske, L. Rezzolla, and K. Schwenzer, *Phys. Rev. Lett.* **120**, 041101 (2018).
- [46] D. Radice, *Astrophys. J.* **838**, L2 (2017).
- [47] M. Shibata and K. Kiuchi, *Phys. Rev. D* **95**, 123003 (2017).
- [48] R. De Pietri, A. Feo, J. A. Font, F. Löffler, F. Maione, M. Pasquali, and N. Stergioulas, *Phys. Rev. Lett.* **120**, 221101 (2018).
- [49] A. Bauswein and H. T. Janka, *Phys. Rev. Lett.* **108**, 011101 (2012).

- [50] S. Bose, K. Chakravarti, L. Rezzolla, B. S. Sathyaprakash, and K. Takami, *Phys. Rev. Lett.* **120**, 031102 (2018).
- [51] J. Clark, A. Bauswein, L. Cadonati, H. T. Janka, C. Pankow, and N. Stergioulas, *Phys. Rev. D* **90**, 062004 (2014).
- [52] K. Takami, L. Rezzolla, and L. Baiotti, *Phys. Rev. Lett.* **113**, 091104 (2014).
- [53] L. Rezzolla and K. Takami, *Phys. Rev. D* **93**, 124051 (2016).
- [54] K. Hotokezaka, K. Kiuchi, K. Kyutoku, T. Muranushi, Y.-i. Sekiguchi, M. Shibata, and K. Taniguchi, *Phys. Rev. D* **88**, 044026 (2013).
- [55] A. Bauswein, N. Stergioulas, and H. T. Janka, *Phys. Rev. D* **90**, 023002 (2014).
- [56] K. Chatziioannou, J. A. Clark, A. Bauswein, M. Millhouse, T. B. Littenberg, and N. Cornish, *Phys. Rev. D* **96**, 124035 (2017).
- [57] G. Lioutas, A. Bauswein, and N. Stergioulas, *Phys. Rev. D* **104**, 043011 (2021).
- [58] J. A. Clark, A. Bauswein, N. Stergioulas, and D. Shoemaker, *Classical Quantum Gravity* **33**, 085003 (2016).
- [59] P. J. Easter, P. D. Lasky, A. R. Casey, L. Rezzolla, and K. Takami, *Phys. Rev. D* **100**, 043005 (2019).
- [60] M. Breschi, S. Bernuzzi, F. Zappa, M. Agathos, A. Perego, D. Radice, and A. Nagar, *Phys. Rev. D* **100**, 104029 (2019).
- [61] P. J. Easter, S. Ghonge, P. D. Lasky, A. R. Casey, J. A. Clark, F. H. Vivanco, and K. Chatziioannou, *Phys. Rev. D* **102**, 043011 (2020).
- [62] T. Soutanis, A. Bauswein, and N. Stergioulas, *Phys. Rev. D* **105**, 043020 (2022).
- [63] M. Breschi, S. Bernuzzi, K. Chakravarti, A. Camilletti, A. Prakash, and A. Perego, [arXiv:2205.09112](https://arxiv.org/abs/2205.09112).
- [64] M. Breschi, R. Gamba, S. Borhanian, G. Carullo, and S. Bernuzzi, [arXiv:2205.09979](https://arxiv.org/abs/2205.09979).
- [65] M. Wijngaarden, K. Chatziioannou, A. Bauswein, J. A. Clark, and N. J. Cornish, *Phys. Rev. D* **105**, 104019 (2022).
- [66] T. Dietrich, A. Samajdar, S. Khan, N. K. Johnson-McDaniel, R. Dudi, and W. Tichy, *Phys. Rev. D* **100**, 044003 (2019).
- [67] K. W. Tsang, T. Dietrich, and C. Van Den Broeck, *Phys. Rev. D* **100**, 044047 (2019).
- [68] G. Ashton *et al.*, *Astrophys. J. Suppl. Ser.* **241**, 27 (2019).
- [69] I. M. Romero-Shaw *et al.*, *Mon. Not. R. Astron. Soc.* **499**, 3295 (2020).
- [70] N. Stergioulas, A. Bauswein, K. Zagkouris, and H.-T. Janka, *Mon. Not. R. Astron. Soc.* **418**, 427 (2011).
- [71] M. Kölsch, T. Dietrich, M. Ujevic, and B. Bruegmann, *Phys. Rev. D* **106**, 044026 (2022).
- [72] S. Khan, S. Husa, M. Hannam, F. Ohme, M. Pürrer, X. Jiménez Forteza, and A. Bohé, *Phys. Rev. D* **93**, 044007 (2016).
- [73] B. Margalit and B. D. Metzger, *Astrophys. J.* **850**, L19 (2017).
- [74] L. Rezzolla, E. R. Most, and L. R. Weih, *Astrophys. J.* **852**, L25 (2018); *Astrophys. J. Lett.* **852**, L25 (2018).
- [75] J. Antoniadis *et al.*, *Science* **340**, 6131 (2013).
- [76] H. T. Cromartie *et al.* (NANOGrav Collaboration), *Nat. Astron.* **4**, 72 (2019).
- [77] T. Dietrich, D. Radice, S. Bernuzzi, F. Zappa, A. Perego, B. Bruegmann, S. V. Chaurasia, R. Dudi, W. Tichy, and M. Ujevic, *Classical Quantum Gravity* **35**, 24LT01 (2018).
- [78] <http://www.computational-relativity.org/> (2018), CoRe Database webpage.
- [79] P. Virtanen, R. Gommers, T. E. Oliphant, M. Haberland, T. Reddy, D. Cournapeau, E. Burovski, P. Peterson, W. Weckesser, J. Bright *et al.*, *Nat. Methods* **17**, 261 (2020).
- [80] K. Kiuchi, K. Kawaguchi, K. Kyutoku, Y. Sekiguchi, and M. Shibata, *Phys. Rev. D* **101**, 084006 (2020).
- [81] A. Nitz, I. Harry, D. Brown, C. M. Biwer, J. Willis, T. D. Canton, C. Capano, T. Dent, L. Pekowsky, A. R. Williamson *et al.*, gwastro/pycbc: Release v2.0.1 of pycbc (2022), [10.5281/zenodo.5825666](https://doi.org/10.5281/zenodo.5825666).
- [82] J. Veitch and A. Vecchio, *Phys. Rev. D* **81**, 062003 (2010).
- [83] J. Skilling, *Bayesian Anal.* **1**, 833 (2006).
- [84] J. S. Speagle, *Mon. Not. R. Astron. Soc.* **493**, 3132 (2020).
- [85] S. Koposov, J. Speagle, K. Barbary, G. Ashton, J. Buchner, C. Scheffler, B. Cook, C. Talbot, J. Guillochon, P. Cubillos *et al.*, joshspeagle/dynesty: v1.2.2 (2022), [10.5281/zenodo.6456387](https://doi.org/10.5281/zenodo.6456387).
- [86] B. Zackay, L. Dai, and T. Venumadhav, [arXiv:1806.08792](https://arxiv.org/abs/1806.08792).
- [87] N. Leslie, L. Dai, and G. Pratten, *Phys. Rev. D* **104**, 123030 (2021).
- [88] L. Dai, T. Venumadhav, and B. Zackay, [arXiv:1806.08793](https://arxiv.org/abs/1806.08793).
- [89] J. Janquart, RelativeBilbying: A package for relative binning with bilby, <https://github.com/lemnis12/relativebilbying> (2022).
- [90] T. Hinderer *et al.*, *Phys. Rev. Lett.* **116**, 181101 (2016).
- [91] K. Kiuchi, K. Kawaguchi, K. Kyutoku, Y. Sekiguchi, M. Shibata, and K. Taniguchi, *Phys. Rev. D* **96**, 084060 (2017).
- [92] K. Kawaguchi, K. Kiuchi, K. Kyutoku, Y. Sekiguchi, M. Shibata, and K. Taniguchi, *Phys. Rev. D* **97**, 044044 (2018).
- [93] L. Wade, J. D. E. Creighton, E. Ochsner, B. D. Lackey, B. F. Farr, T. B. Littenberg, and V. Raymond, *Phys. Rev. D* **89**, 103012 (2014).
- [94] J. Miller, L. Barsotti, S. Vitale, P. Fritschel, M. Evans, and D. Sigg, *Phys. Rev. D* **91**, 062005 (2015).
- [95] B. P. Abbott *et al.* (KAGRA, LIGO Scientific, Virgo Collaborations), *Living Rev. Relativity* **21**, 3 (2018).
- [96] T. Akutsu *et al.* (KAGRA Collaboration), *Prog. Theor. Exp. Phys.* **2021**, 05A101 (2021).
- [97] K. Somiya (KAGRA Collaboration), *Classical Quantum Gravity* **29**, 124007 (2012).
- [98] Y. Aso, Y. Michimura, K. Somiya, M. Ando, O. Miyakawa, T. Sekiguchi, D. Tatsumi, and H. Yamamoto (KAGRA Collaboration), *Phys. Rev. D* **88**, 043007 (2013).
- [99] M. Saleem *et al.*, *Classical Quantum Gravity* **39**, 025004 (2022).
- [100] K. Ackley *et al.*, *Pub. Astron. Soc. Aust.* **37**, e047 (2020).
- [101] L. Barsotti, E. McCuller, M. Evans, and P. Fritschel, The A+ design curve, <https://dcc.ligo.org/LIGO-T1800042/public> (2018).
- [102] S. Hild *et al.*, *Classical Quantum Gravity* **28**, 094013 (2011).

- [103] M. Evans, J. Harms, and S. Vitale, Exploring the sensitivity of next generation gravitational wave detectors, <https://dcc.ligo.org/LIGO-P1600143/public> (2016).
- [104] Y. Michimura, K. Komori, Y. Enomoto, K. Nagano, and K. Somiya, Example sensitivity curves for the KAGRA upgrade (2020), <https://gwdoc.icrr.u-tokyo.ac.jp/cgi-bin/DocDB/ShowDocument?docid=9537>.
- [105] V. Srivastava, D. Davis, K. Kuns, P. Landry, S. Ballmer, M. Evans, E. D. Hall, J. Read, and B. S. Sathyaprakash, *Astrophys. J.* **931**, 22 (2022).
- [106] <https://www.gw-openscience.org>.
- [107] J. Veitch *et al.*, *Phys. Rev. D* **91**, 042003 (2015).
- [108] LIGO Scientific Collaboration, LIGO Algorithm Library - LALSuite, 10.7935/GT1W-FZ16.